

**THE IMPACT OF SPACEBORNE DOPPLER RADAR OBSERVATIONS
ON THE SIMULATION OF A TROPICAL CYCLONE**

by William E. Lewis

a dissertation submitted in partial fulfillment of
the requirements for the degree of
Doctor of Philosophy
(Atmospheric and Oceanic Sciences)

at the
UNIVERSITY OF WISCONSIN-MADISON
2007

UMI Number: 3261526

INFORMATION TO USERS

The quality of this reproduction is dependent upon the quality of the copy submitted. Broken or indistinct print, colored or poor quality illustrations and photographs, print bleed-through, substandard margins, and improper alignment can adversely affect reproduction.

In the unlikely event that the author did not send a complete manuscript and there are missing pages, these will be noted. Also, if unauthorized copyright material had to be removed, a note will indicate the deletion.

UMI[®]

UMI Microform 3261526

Copyright 2007 by ProQuest Information and Learning Company.

All rights reserved. This microform edition is protected against unauthorized copying under Title 17, United States Code.

ProQuest Information and Learning Company
300 North Zeeb Road
P.O. Box 1346
Ann Arbor, MI 48106-1346

A dissertation entitled

**The Impact of Spaceborne Doppler Radar Observations
on the Simulation of a Tropical Cyclone**

submitted to the Graduate School of the
University of Wisconsin-Madison
in partial fulfillment of the requirements for the
degree of Doctor of Philosophy

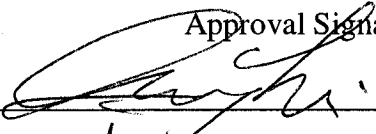


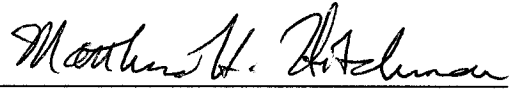
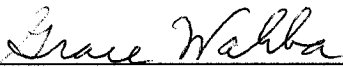
by

William E. Lewis

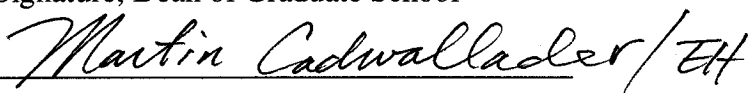
Date of Final Oral Examination: 04/30/07

Month & Year Degree to be Awarded: May 2007

Approval Signatures of Dissertation Committee

Signature, Dean of Graduate School



ABSTRACT

Tropical cyclones (TC) present a tremendous challenge for numerical weather prediction (NWP). Poorly specified initial conditions (i.e. model analyses) are one of the primary sources of forecast error, and high resolution observations are needed to rectify the problem. A geostationary Doppler radar instrument, NEXRAD-In-Space (NIS), has been proposed for this very purpose. A set of observing system simulation experiments (OSSE) is conducted to assess the potential role of data from NIS in improving prediction of TC via improved representation of the TC in the model analysis.

Using the University of Wisconsin Nonhydrostatic Modeling System (UW-NMS) together with an ensemble Kalman filter (EnKF), it is demonstrated that, for a typical Atlantic basin TC, NIS-observed Doppler radial velocity (V_R) and equivalent reflectivity factor (Z_e) are effective in significantly reducing analysis errors. When computed over the entire grid, the degree of improvement ranges from 20 to 80 percent relative to the control (CTL) simulation, while a more homogeneous degree of improvement (50 to 80 percent) is demonstrated at locations where observations have been assimilated. Furthermore, when examination of observation impact is restricted to those surface regions with significant weather ($V_{\text{surf}} > 34$ kt and/or rain rate > 12.5 mm h⁻¹), a nearly uniform improvement of 60 to 80 percent is apparent. In general, a four to six hour assimilation window is sufficient to achieve statistical convergence (i.e. produce errors that are asymptotic relative to control).

In order to determine the degree to which the improved analysis leads to improved forecast results, a 48-hour integration is initialized from an analysis produced by assimilating both V_R and Z_e . Significant impact on both intensity and track are noted, with a 65 percent reduction in intensity error and 56 percent reduction in track error relative to CTL over the forecast period. In general, errors relating to surface wind are more effectively reduced than those relating to rain rate, as is evident from Brier Skill Scores (BSS) computed for a number of wind and rain rate thresholds.

ACKNOWLEDGEMENTS

Seldom, I imagine, do the debts of one's gratitude accrue so quickly and to such a staggering degree as when engaged in a course of work such as the one just completed. In a proverbial sense the road has indeed been a long one, but it has likewise been peopled by reliable guides and fellow travelers, each of whom have in their own ways contributed to this journey having reached its terminus at long last. Most importantly, every moment of the way unfolded with the promise that this conclusion would be met amongst those I cared for most; this, above all else, has been the fuel on which I've traveled.

For their inspiration at the beginning, I wish to thank Drs. Susan Libes and Randall Wells of Coastal Carolina University. I also wish to thank the UW's Dr. Zhengyu Liu, from whom I learned much about the dynamics of atmosphere and ocean as well as the importance of triple-checking even the simplest lines of FORTRAN code. The members of my PhD committee – Drs. Ralf Bennartz, Matt Hitchman, Michael Morgan and Grace Wahba – deserve especial commendation for shaping and guiding my research toward a successful end. The same can be said for my advisor, Dr. Greg Tripoli, and I thank him deeply for affording me both the opportunity and independence to structure and organize things as I saw fit. In a complementary fashion am I indebted to Pete Pokrandt, Connie Linehan and Toni Sumner-Beebe for their skill in crafting order from the very real chaos of network computing and graduate student life. If I've been able to run models, meet deadlines and submit the proper forms – documentary evidence

of this journey's completion – then they deserve the credit. Perhaps one could imagine better guides than these, but I cannot.

Among my fellow travelers, I would especially like to thank Tania Casal, Marek Rogal, Monica Harkey, Howard Berger as well as all my compatriots in the Tripoli research group. On an excursion of this length, one learns quickly to appreciate the value of companionship and theirs has always been true and cordial.

And then of course there are those who wait expectantly at journey's end. Among this gathering are those to whom the greatest debts are owed, and I begin with three who are not here to partake in the celebration. Let me then celebrate them. My grandmothers, Ava Lewis and Lila Shay, for biscuits and sweet tea on impossibly long summer afternoons and for riveting stories of hurricanes long past; my mother-in-law Irene Roy, for an introduction to *gaufres* in fin de siècle Paris. All are cherished and inspirational memories. I would also like to thank my father-in-law Dr. Prodyot Roy, fuel-cell pioneer, for his counsel and assistance in so many ways over the course of the last seven years.

The depth of gratitude toward my family, in South Carolina and elsewhere, is as close to boundless as one can imagine. I thank my sisters Cynthia, Diana and Patricia and all my nieces, nephews, in-laws, aunts and uncles for their inspiration from afar all these years I've been away from home. I also want to thank my Uncle Bill and Aunt Connie for their kindness and support from a somewhat more proximal location.

I thank my mom and dad for everything; my mom especially for her unceasing fascination with the weather, communicated to me in childhood and nurtured to this very day; and my dad for instilling in me an early and abiding faith in God that has carried me

thus far through life's ups and downs. Without them both, it is difficult to imagine having reached the point of writing these acknowledgments.

And finally I thank my wife Nina and my son Logan, the twin stars that hold me in firm, joyously eccentric orbit: Nina, a source of motivation, inspiration and love that is daily renewed; and Logan, the wellspring of my finer self, a source the depth and inexhaustibility of which he hasn't yet begun to realize.

TABLE OF CONTENTS

ABSTRACT	i
ACKNOWLEDGEMENTS	iii
LIST OF FIGURES	viii
LIST OF TABLES	x
1. INTRODUCTION	1
I. THE TROPICAL CYCLONE PROBLEM(S).....	1
II. OBSERVING AND PREDICTING TCS: PAST, PRESENT AND FUTURE	2
III. TOWARD A PROBABILISTIC FRAMWORK FOR NUMERICAL WEATHER PREDICTION (NWP)	6
2. NEXRAD-IN-SPACE	11
3. HURRICANE BETA (2005)	18
I. SYNOPTIC HISTORY	18
II. IMPACT ON CENTRAL AMERICA	19
III. OFFICIAL FORECAST STATISTICS	20
4. MODEL DESCRIPTION AND EXPERIMENT METHODOLOGY	25
I. MODEL DESCRIPTION.....	25
II. SIMULATION SPECIFICS	26
III. OBSERVING SYSTEM SIMULATION EXPERIMENT (OSSE) METHODOLOGY	27
IV. EMULATING THE DISPARITY BETWEEN MODEL AND REAL ATMOSPHERE	30

V. GENERATION OF ENSEMBLE INITIAL AND BOUNDARY CONDITIONS	32
VI. EVALUATION METRICS	34
VII. ENSEMBLE KALMAN FILTER (ENKF).....	35
5. ANALYSIS IMPACT.....	42
I. TRACK AND INTENSITY.....	42
II. SURFACE FIELDS	44
III. ERRORS AT OBSERVATION LOCATIONS	45
IV. GRID-AVERAGED ERRORS	47
V. ERRORS AT LOCATIONS WITH SIGNIFICANT WEATHER.....	48
VI. LAYER-AVERAGED ERRORS.....	49
VII. CONCLUSIONS.....	51
6. FORECAST IMPACT	62
I. CTL AND VRZ TRACK AND INTENSITY ERRORS	63
II. TIME SERIES OF SURFACE WIND AND RAIN AT 6 STATIONS	65
III. FORECAST SKILL	66
IV. CONCLUSIONS.....	69
7. CONCLUDING REMARKS AND FUTURE WORK.....	83
REFERENCES	88

LIST OF FIGURES

1.1	NHC track and intensity forecast error statistics for the period 1990-2005	9
1.2	Intensity forecast skill of the 2006 GFDL hurricane model	10
2.1	Illustration of the NIS spiral scan strategy.....	16
2.2	Partitioning of NIS V_R for three separate scenarios.....	17
3.1	Track of Hurricane Beta (2005)	21
3.2	Intensity time series for Hurricane Beta (2005).....	22
3.3	Satellite view of Beta near maximum intensity	23
4.1	Grid configuration for the UW-NMS simulations	40
4.2	Ensemble initial and boundary condition generation	41
5.1	Tracks of TR, CTL, Z, VR, and VRZ over the assimilation window	54
5.2	Intensity (MSLP) of TR, CTL, Z, VR and VRZ over the assimilation window.....	55
5.3	Sea-level pressure and surface wind for TR, CTL, VR, Z and VRZ	56
5.4	RMSE for Z,VR and VRZ relative to CTL at observation locations only	57
5.5	As in 5.4, but computed for each gridpoint in the inner nest.....	58
5.6	As in 5.4 and 5.5, but computed for surface locations with significant weather	59
5.7	Layer-averaged RMSE relative to CTL at observation locations only	60

5.8 As in 5.7, but computed for each gridpoint in the inner nest.....	61
6.1 TR and CTL forecast tracks	71
6.2 TR and CTL forecast intensities.....	72
6.3 Track and intensity errors for CTL ensemble forecast	73
6.4 Track and intensity errors for VRZ ensemble forecast	74
6.5 TR and VRZ forecast tracks	75
6.6 TR and VRZ forecast intensities	76
6.7 Six surface locations for which time series of wind and rain are examined.....	77
6.8 Time series of wind and rain for 6 surface stations.....	78
6.9 Brier Skill Scores (BSS) for 3 wind and 3 rain rate thresholds	82

LIST OF TABLES

2.1	NEXRAD In Space (NIS) design and performance parameters	15
3.1	NHC Forecast Error Statistics for Hurricane Beta	24
4.1	Relevant simulation details for TR, CTL, Z, VR and VRZ.....	39
6.1	Correlations between TR and CTL, TR and VRZ and their significance	80
6.2	Threshold criteria used in computing Brier Skill Scores (BSS) for VRZ	81

Chapter 1

Introduction

“In science one tries to tell people, in such a way as to be understood by everyone, something that no one ever knew before. But in poetry, it's the exact opposite.”

Paul Dirac

i. The tropical cyclone problem

The perspicacity of Dirac's pronouncement notwithstanding, there can be no question that tropical cyclones have, from ancient times to present, inspired poet and scientist alike. Louie and Liu (2003) report that at least as early as AD 712, the poet Song Zhi-wen writes of a tropical-cyclone-like storm affecting Guangdong, while 15 years later Gu Kuang writes to his cousin to beware the *jufeng* should he chance to encounter one on his sea voyage to Xin Luo. *Jufeng* is the etymological predecessor of *taifeng*, which has in turn evolved into the word typhoon, a once-regional appellation nowadays nearly as familiar to the world at large as it is to those who live along the Western Pacific rim.

Gu Kuang's admonition to his cousin is easy to understand when we consider that the Western Pacific basin is the most active region in the world as regards tropical cyclones, each year on average producing more than 20 of these potentially devastating storms (Gray, 1979). Elsewhere, tropical cyclones occur over the tropical and subtropical oceans of the world (though with extreme rarity south of the equator in the Atlantic) and are menaces to life and property over the open ocean as well as to all adjacent land areas,

for surface wind speed in an intense hurricane may approach 100 m s^{-1} and rainfall totals may exceed 1 m over a several day period. Indeed, as the 2005 North Atlantic hurricane season demonstrated, these intense vortical storms are capable of spreading destruction and loss of life across wide geographical areas in relatively short periods of time (Beven, 2006). While questions of climate-change impact on this and future hurricane seasons are contentious (e.g. Emanuel, 2005; Gray, 2005), there is general consensus on the importance of working to improve forecasts of tropical cyclone formation, intensity change and precipitation¹. These three challenges form the core of what may be termed the tropical cyclone problem. A fourth challenge is obtaining adequate observations of the storm and its immediate environment, and the next section provides a more rigorous discussion of why the observation issue is of particular importance when endeavoring to attack the tropical cyclone problem.

ii. Observing and predicting tropical cyclones: past, present and future

Before embarking on an examination of the difficulties with both observation and prediction of tropical cyclones, it will be useful to pause and first rigorously define what a tropical cyclone is (and, perhaps as importantly, what it isn't). Holland (1993) defines a tropical cyclone as a non-frontal low-pressure system of synoptic scale with organized convective (i.e. thunderstorm) structure. This non-frontal character essentially distinguishes tropical cyclones from the familiar baroclinic systems of midlatitudes.

Implicit in that structural difference is a similar disparity in the source of energy that

¹ 2000: policy statement: Hurricane Research and Forecasting. Bulletin of the American Meteorological Society: Vol. 81, No. 6, pp. 1341–1347

drives the storms: large-scale temperature gradients in the case of frontal cyclones; the thermodynamic disequilibrium between ocean and atmosphere in the case of tropical cyclones (Emanuel, 1986). Whether it occurs in the Atlantic or Eastern Pacific (where it is known as a hurricane), over the Western Pacific (typhoon) or the South Pacific or Indian Oceans (simply tropical cyclone), enthalpy flux from the ocean surface is the lifeblood of this phenomenon, and as soon it moves over land, it begins to weaken rapidly (although the rate of weakening may vary widely and may not necessarily be accompanied by a corresponding decrease in rainfall – the latter being a very important consideration in areas prone to flash flooding).

Thus much do we know about the mechanics and thermodynamics of the tropical cyclone heat engine, and in this age of myriad satellites, cable news and supercomputers, it is easy to forget that tropical cyclones were once (and in some sense still are) poorly understood and observed. Until Lt. Col. Joe Duckworth, acting on a dare from a fellow officer, took his AT-6 into the eye of a hurricane off the Texas coast in 1943 (thus beginning the era of aircraft reconnaissance), the only observations of hurricanes were those from eyewitnesses, on the ground or at sea, unlucky enough to find themselves in the path of the storm (Sumner, 1943). Inspired by Duckworth's success, the U.S. Navy and U.S. Air Force embarked on hurricane reconnaissance programs that did, and, in the case of the Air Force, continue to provide valuable observations of hurricanes. The 1950s ushered in the space race and with it the advent of weather satellites. From the humble TIROS with its grainy infrared images to the high-resolution instruments of today, satellites have revolutionized the way we think about our planet in general and about

weather and tropical cyclones in particular. Not only did storms become visible that might never have been detected before, but the possibility of using the measurements made by satellite radiometers to help initialize numerical weather prediction (NWP) models became a reality.

So begins the era of satellite data assimilation and with it a vast improvement in the forecasts made by the global models run at the National Centers for Environmental Prediction (NCEP) and elsewhere. The models that are used by the various tropical cyclone forecast centers worldwide depend to a greater or lesser degree on the global model output, and, not unexpectedly, the general improvement seen in the global models is reflected in tropical cyclone forecasts as well. Figure 1.1 shows annual mean errors for forecasts of hurricane track (1.1a) and intensity (1.1b) issued by the National Hurricane Center (NHC) for the years 1989 to 2005. Two things are immediately obvious. First, hurricane track prediction has gotten much better over that 16-year period (note especially that 48-hour forecasts in 2005 are as good as 24-hour forecasts in 1989, and 72-hour forecasts are better in 2005 than 48-hour forecasts were in 1989!) Certainly this is a success story, and the impact of satellite (and other) data assimilation and model improvement should receive the credit. The next obvious fact is the lack of a corresponding success story for intensity forecasts. The trend lines show meager improvement in the 48 and 72-hour forecasts and essentially no trend at 24 hours. The reason is that the processes which govern the intensity of tropical cyclones occur at much smaller scales than do those which control track. The current generation of operational models (both global and regional) is in general too coarse to adequately represent the

convective-scale dynamics and scale-interaction processes that drive tropical cyclone intensity changes. In addition, the lack of reliable, readily available high-resolution observations (as well as the means to incorporate them into the models in a timely manner) ensures that any model forecast quickly departs from nonlinear reality. However, the times are changing.

For instance, Bender et al. (2006) demonstrated that using more sophisticated physics parameterizations, as well as improving the representation of key upper-ocean features (i.e. the loop current) in the Geophysical Fluid Dynamics Laboratory (GFDL) hurricane model resulted in significant improvement when re-run on a number of cases from the 2004 and 2005 Atlantic seasons (figure 1.2). These results support the assertion of Houze et al. (2007) that high-resolution models with an interactive ocean are necessary to capture the essential structural evolution of the near-hurricane environment and hurricane inner core that result in eyewall replacement cycles (a leading cause of currently unpredictable intensity change in intense hurricanes). Houze et al. also argue that real-time assimilation of storm-scale observations from the near-hurricane environment will likely be a key component of improved forecasts of intensity change.

While targeted observations (using either conventional or unmanned reconnaissance aircraft) are one possible means of accomplishing this task, the one under examination here is a stationary platform capable of providing broad, regular coverage of the key tropical cyclone basins. This instrument, known as NEXRAD In Space (NIS) (Im et al., 2003) would be a geostationary Doppler radar capable of providing hourly (or better) observations at horizontal scales of 12 to 14 km and with a vertical resolution of

300 m. Demonstrating that NIS observations of equivalent radar reflectivity, Z_e , and Doppler radial velocity, V_R , would be capable of providing positive impact in forecasts of tropical cyclone track and intensity will be the focus of this research.

iii. Toward a probabilistic framework for numerical weather prediction (NWP)

The NIS data are fated, as all measurements, to some degree of corruption by noise. Given that NWP models themselves are subject to multiple sources of error, it is suggested here that tropical cyclone prediction (indeed *all* weather prediction) is most naturally phrased in probabilistic terms. What is needed, then, is a means not only of integrating measurements into the model (e.g. the data assimilation problem), but a way to take account of the associated forecast errors. Such an algorithm, the Kalman Filter (KF), exists but is not tractable for high-dimensional problems such as the one at hand. To that end, a Monte Carlo implementation of the KF will be pursued.

The Kalman filter (Kalman, 1960) is a finite-dimensional, recursive algorithm for propagating the state probability density function (PDF) of a linear, Gaussian system forward in time, subject to the conditioning influence of noisy observational data. The model dynamics tend to diffuse probability with time (i.e. increase the variance associated with an estimate), and the observations act to counteract this diffusion (i.e. reduce the variance). This dynamic equilibrium between model and measurement is a powerful one and has led to the KF enjoying successful application in a startlingly wide-range of disciplines, from space travel to economics.

Despite this success, the requirement of linear model dynamics would seem to impose an insurmountable obstacle to the application of the KF to the tropical cyclone prediction problem. One possible solution, the so-called extended Kalman filter (EKF) (e.g. Bucy and Senne, 1971) uses linearized model operators. While the EKF produces acceptable results in some instances, it suffers from another of the KF's problematic features: namely the requirement of propagating the *entire* state covariance matrix (Gelb, 1974). Given that a typical NWP will have 10^6 or 10^7 elements in its state vector, the covariance matrix would then have 10^{12} to 10^{14} elements. The storage requirements for such arrays are prohibitive, let alone the computational cost.

Thankfully, a computationally tractable algorithm exists: the ensemble Kalman filter (EnKF) (Evensen, 1994). The details of the EnKF will be presented in a later chapter, but it is worth mentioning here that not only is the logistical problem of covariance propagation solved, the very method of solution allows for the covariances to evolve in accord with the fully nonlinear dynamics of the model. Given what we know about the current challenges facing TC intensity prediction, this property of the EnKF makes it very appealing indeed.

Chapter 2 provides a brief description of the NIS instrument, highlighting its novel features and advantages over present-day geostationary (GEO) and low-earth orbiting (LEO) instruments. Chapter 3 presents Beta, a hurricane from the 2005 Atlantic season whose case will be used to demonstrate the impact of NIS data. Chapter 4 gives a summary of the numerical model (UW-NMS) as well as the experiment design (including the simulation and assimilation details, and the OSSE methodology). Chapter 5 presents

the results of a near-perfect model experiment, demonstrating the NIS impact on the analysis phase. Chapter 6 demonstrates forecast impact, and a summary of the results (as well as plans for future work) are presented in chapter 7.

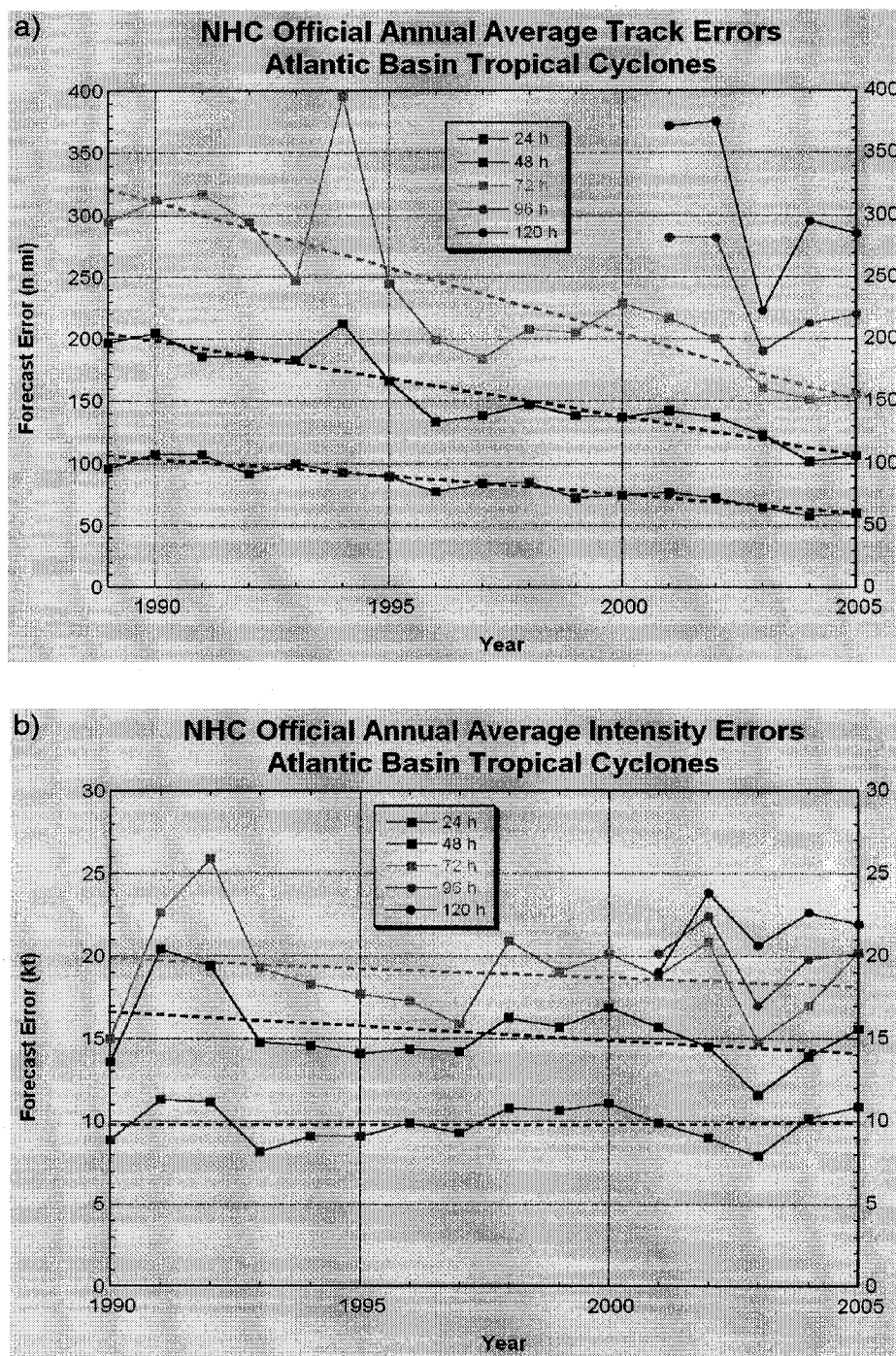


FIG. 1.1: Annual errors for (a) track and (b) intensity for forecasts issued by the National Hurricane Center (NHC) for Atlantic basin tropical cyclones of tropical storm strength or greater (sustained wind speed ≥ 34 kt) (figure courtesy of NHC).

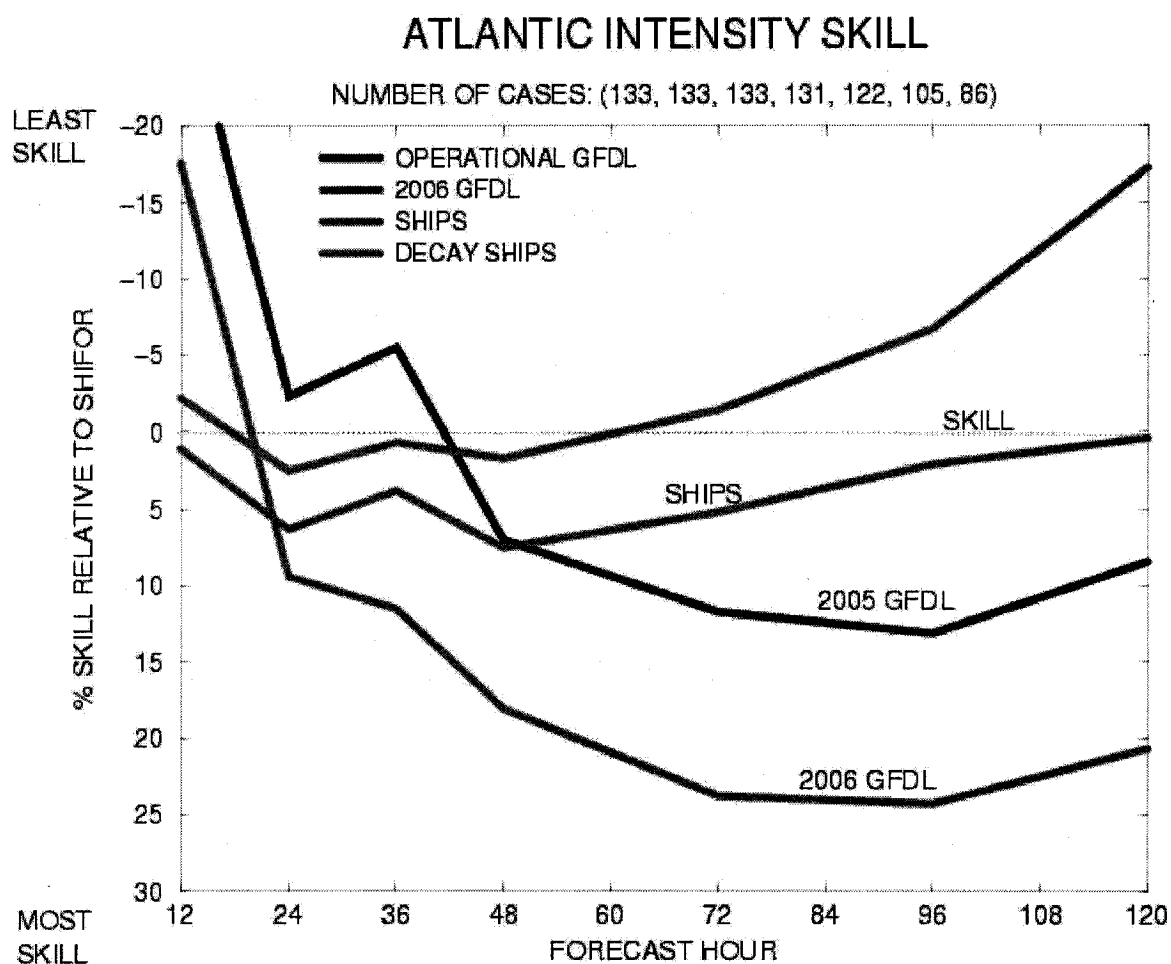


FIG. 1.2: A comparison of the skill of two statistical models (SHIPS, DSHIPS) and two versions of the Geophysical Fluid Dynamics Laboratory (GFDL) dynamical hurricane model. The 2006 version of the GFDL exhibits an improvement of 10 percent over the 2005 version when tested on the same cases (from Bender et al., 2006).

Chapter 2

NEXRAD In Space

The potential of employing dopplerized Ka-band radar for cloud physics research has been recognized since at least the 1980s (Hobbs et al., 1985), but the idea of placing a dopplerized Ka-band instrument in geosynchronous orbit for the explicit purpose of monitoring tropical cyclones is completely novel. This section will provide a brief outline of the design and performance parameters of the NIS instrument, a summary of which may be found in table 2.1; readers interested in a more detailed treatment are referred to the papers by Im et al. (2003) or Lin et al. (2006).

To some, it might seem as if the skies are quite literally filled with weather satellites. Indeed, geostationary satellites have the vast majority of earth under surveillance at 30 minute intervals, and constellations of low-earth orbiting satellites (LEO) race above the globe providing continuous albeit narrow swaths of high-resolution imagery. Yet despite this litany of remote sensing instruments and the coverage it implies, tropical cyclones are still rather poorly observed. There are two principal reasons.

First, by their very nature, tropical cyclones are convectively active. This entails a large output of dense cirrostratus cloud that often makes it difficult for a conventional geostationary satellite to observe below the tropopause. The profile of a hurricane in this context is a two-dimensional silhouette, revealing little of the important processes underway in the layers below. This difficulty may be overcome to some degree if observations are made in the microwave (either passively or actively), and a more

representative, three-dimensional picture can then emerge. A number of satellite instruments (TRMM PR, SSMI, AMSU, etc.) do exactly this, providing a valuable set of observations in the process (e.g. Brueske and Velden, 2003). However, each of these instruments sits aboard a LEO satellite and is therefore hampered by a rather narrow footprint / swath and a return time on the order of 12 to 24 hours. Therefore, the current GEO and LEO deployment, separately or together, offers a broad yet unsatisfactory sampling of tropical cyclones.

To mitigate these shortcomings, NIS would essentially combine the strengths of the GEO and LEO platforms, and then add the extra advantage of Doppler capability. Geosynchrony offers the fidelity of repeatable coverage of a specified area. In order to achieve the desired horizontal and vertical resolutions (~13km and 300m, respectively) at GEO altitude, a spherical antenna with an aperture of 28 m is required. An innovative spiraling dual-feed is employed to cover a disc on the earth's surface with a diameter of 5,300 km, which results in coverage to approximately 23° north/south of the equator (figure 2.1). If NIS were to be deployed at 82.5° W, for example, this would permit observation of the entire Caribbean sea and much of the main development region (MDR) in the eastern Pacific (one might also imagine a deployment in the central tropical Atlantic, say at 40° W, which would allow the Atlantic MDR to be observed in its entirety). The time required to complete a spiral scan is one hour, thus providing surveillance of the tropics (or some subsection thereof) at a temporal resolution vastly superior to low-earth orbiting (LEO) satellites.

Active sampling in the microwave spectrum offers the advantage of three-dimensional profiling of the storm, unhampered as are GEO instruments by intervening cloud layers. NIS would operate at 35 GHz (i.e. Ka band), and would be further augmented by Doppler capability. Unlike conventional ground-based Doppler instruments that provide measurements of radial velocity, V_R , which can be used to profile the horizontal wind field, NIS, by virtue of its position in space, would provide profiles of the vertical motion field (more properly, the fall speed field, where fall speed is the difference between the hydrometeor terminal velocity, v_T , and the vertical velocity, w).

However, it must be noted that for substantial horizontal motion (such as occurs in mature tropical cyclones) the contribution to V_R from the horizontal wind components u and v will be non-trivial for off-nadir scans. To illustrate this point, we can decompose V_R into its horizontal and vertical components, V_v and V_h , which will be functions of the incidence angles in the north and south directions (θ and γ , respectively). In particular, we have:

$$V_v = (v_T - w) \cos \theta \cos \gamma, \quad (2.1)$$

$$V_h = \sqrt{u^2 \cos^2 \theta \sin^2 \gamma + v^2 \sin^2 \theta \cos^2 \gamma}. \quad (2.2)$$

Figure 2.2 shows the relative fraction of vertical component, V_v , to total V_R plotted against degrees latitude/longitude away from the satellite subpoint for three separate scenarios. The first, shown in 2.2a, depicts the case when fall speed and horizontal speed have equal magnitude (i.e. $|v_T - w| = (u^2 + v^2)^{1/2}$). In this case it can be seen that for all scan angles of interest, 70 percent or greater of the NIS radial velocity is composed of the

vertical component. An even greater proportion is realized in an instance of intense convection under quiescent background flow (i.e. $|v_T - w| = 10(u^2 + v^2)^{1/2}$) as depicted in 2.2b. Here, the contribution from the vertical component is never less than 95 percent in the NIS field of view. A much different picture emerges, however, if the case of an intense tropical cyclone (i.e. $|v_T - w| = 0.1(u^2 + v^2)^{1/2}$) is considered, as is shown in 2.2c. For locations on the globe more than 10 degrees north or south of the equator, the Doppler radial velocity is composed almost entirely (greater than 90 percent) of the horizontal component. While it is true that individual hot towers within intense TCs will provide brief exceptions to this fractionation, the fact that most TCs (and nearly all intense TCs) occur more than 10 degrees poleward of the equator must lead one to conclude that, on average, one may not expect to directly sample the vertical motion fields within intense tropical cyclones without considerable “contamination” by the horizontal wind field.

This caveat notwithstanding, the combined coverage, frequency and quality of observation provided by NIS would be unrivaled and would carry the potential for great insight into the physical processes at work across the full spectrum of the tropical cyclone life cycle. The impact on numerical weather prediction ought to be cast in rigorous, quantitative terms, and so the following chapters will establish the modeling and experimental framework necessary to assess the impact of NIS observations on simulations of tropical cyclones. First, however, a suitable TC case will need to be identified.

TABLE 2.1: NEXRAD In Space (NIS) design and performance parameters.

Parameter	Value
Frequency (GHz)	35
Range Resolution (m)	300
Horizontal Resolution (km)	12 (nadir), 14 (4°)
Disk Coverage (km)	5300
Pulse Compression Sidelobes (dB)	-30
Antenna Aperture (m)	28
Beamwidth (deg.)	0.02
Minimum Detectable Reflectivity (dBZ)	5
Doppler Precision (m/s)	0.3

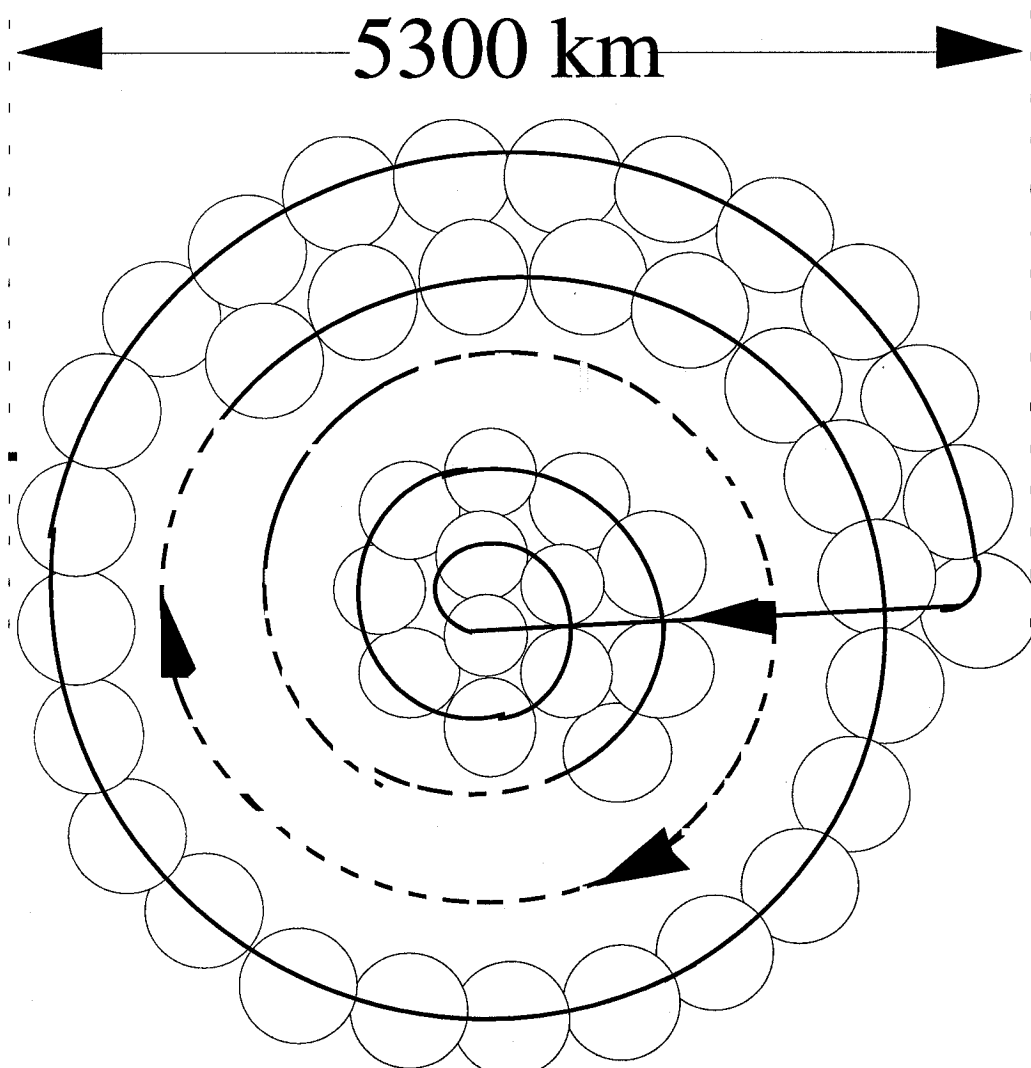


FIG. 2.1: Illustration of the NIS spiral scan. Note that the scan illuminates a disk of radius 5,300 km (approximately $\pm 23^\circ$ latitude/longitude) on the earth's surface.

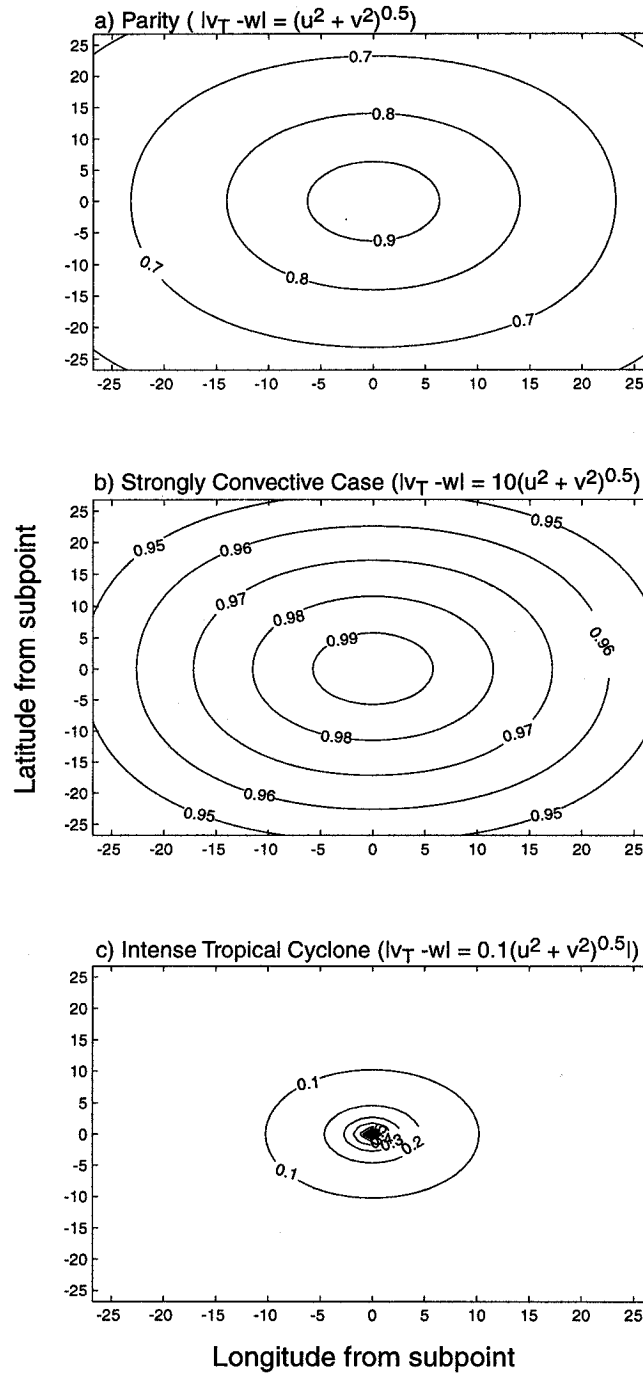


FIG. 2.2: The relative proportion of vertical component, V_V , to total Doppler radial velocity, V_R , under three separate assumptions: (a) parity, (b) strong convection in quiescent background flow, (c) intense tropical cyclone.

Chapter 3

Hurricane Beta (2005)

Beta was a typical October hurricane in most respects, developing in the western Caribbean Sea on 26 October and briefly attaining major hurricane status before landfall on the Nicaraguan coast on 30 October. This, together with the fact that the entire life cycle transpired over a relatively small geographical area that is favorably situated with regard to a potential NIS field of view, makes Beta an appealing candidate. This chapter briefly sets out the synoptic history of Beta, summarizes its effects on Central America, and provides a discussion of the statistics associated with the National Hurricane Center (NHC) forecasts for Beta. Nearly all the material presented here is drawn from the tropical cyclone report by Pasch and Roberts (2006).

i. Synoptic history

As do many Atlantic tropical cyclones, Beta developed from a disturbance that can be traced back to an African easterly wave. In this instance, it is interesting to note that the particular disturbance that gave rise to Beta also spawned tropical storm Alpha a few days earlier. The track shown in figure 4.1 reveals a slow northward motion for several days followed by a westward turn toward Central America beginning on 29 October. This motion can be understood in terms of the evolving synoptic-scale flow over North America, which was dominated by a broad 500 hPa trough for the first few days of Beta's existence. The trough gradually moved off the mid-Atlantic coast, resulting in 500

hPa height rises over the Gulf of Mexico which turned Beta westward at a gradually increasing forward speed. Later, Beta came under the influence of a strong, mid/upper level anticyclone centered over the eastern Pacific and turned to the southwest, approximately 12 hours before landfall.

The intensification of Beta was likewise languid, with a deepening rate of only about 10 hPa per day over the first 72 hours, followed by a more substantial intensification that began approximately 18 hours prior to landfall (figure 4.2). The pressure is estimated to have reached a minimum value of 962 hPa at 6Z on 30 October. Figure 4.3 shows four separate satellite perspectives of Beta near maximum intensity. The two top panels are views from the GOES infrared sensor and show a classic pattern of cold (in the image on the top left, white) cloud tops. The two lower panels are microwave imagery from SSM/I. The one on the lower left shows the horizontally polarized 85 GHz brightness temperatures, often used as a proxy for rain rate. Shortly after these images were taken, northeasterly shear (stemming from the eastern Pacific anticyclone mentioned above) began to impact Beta and the cyclone started to fill, eventually reaching the coast near 12Z with a pressure of 970 hPa.

ii. Impact on Central America

Despite the indolent course of motion and a trajectory that kept Beta close to and then over significant topography, the impact from fresh-water flooding appears not to have been significant. The maximum recorded rainfall was 21.82 inches at Trujillo, and many locations in Nicaragua and Honduras reported much less. Remarkably, there was

no loss of life attributed to the cyclone. The fortuitously mild impact can perhaps in part be attributed to Beta's relatively small size (tropical storm force winds covered an area roughly 100 km in diameter) and the rapid decrease in organization after landfall. In fact, the dissipation of Beta over Central America was remarkably swift, essentially reaching completion within 18 hours of landfall.

iii. Official forecast statistics

The track and intensity forecasts for Beta mirror the larger problems of tropical cyclone track and intensity forecasting as outlined in chapter one. The track forecasts for Beta were excellent, with errors less than the most recent ten-year mean at each verifying time (Table 4.1). This can in large part be attributed to the success of the global models in depicting and forecasting the evolving steering flow over the western Caribbean. Such is not the case for intensity. Table 4.1 shows that the NHC intensity forecasts were worse than the ten-year mean at 12, 24 and especially 72 hours. The difficulties of intensity forecasting are well recognized, and provide one of the primary motivations for the research undertaken here and elsewhere.

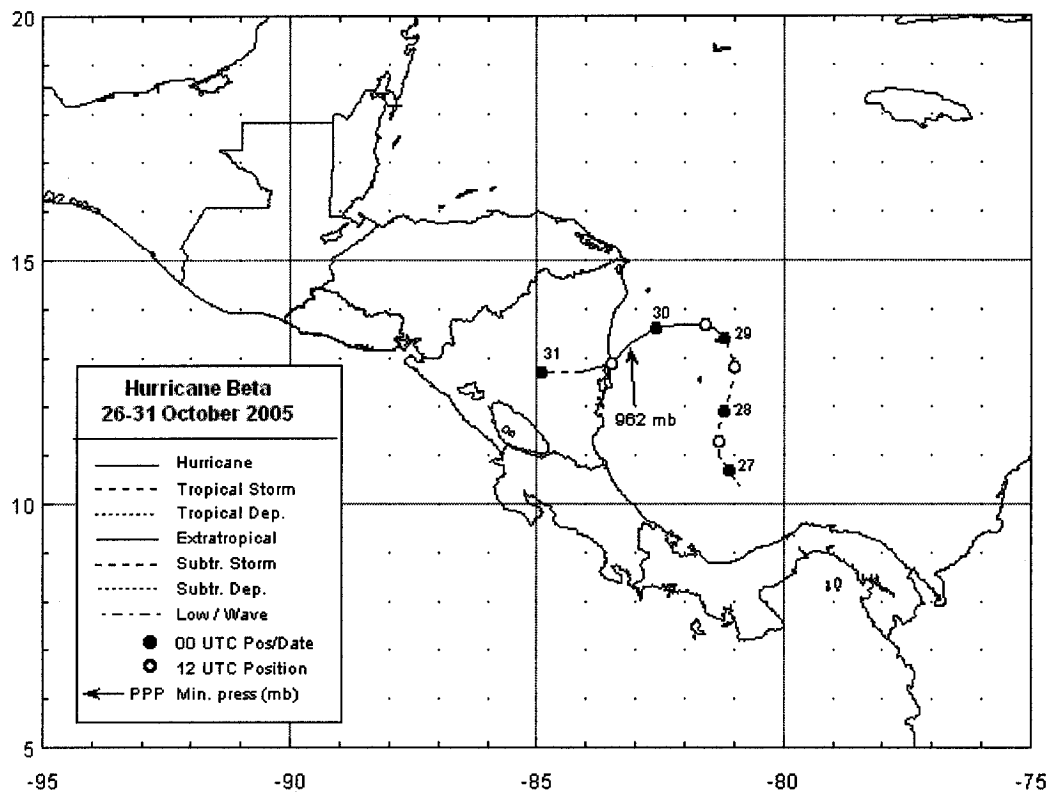


FIG. 3.1: Track of hurricane Beta as given by the NHC best track analysis. (Figure courtesy of Richard Pasch.)

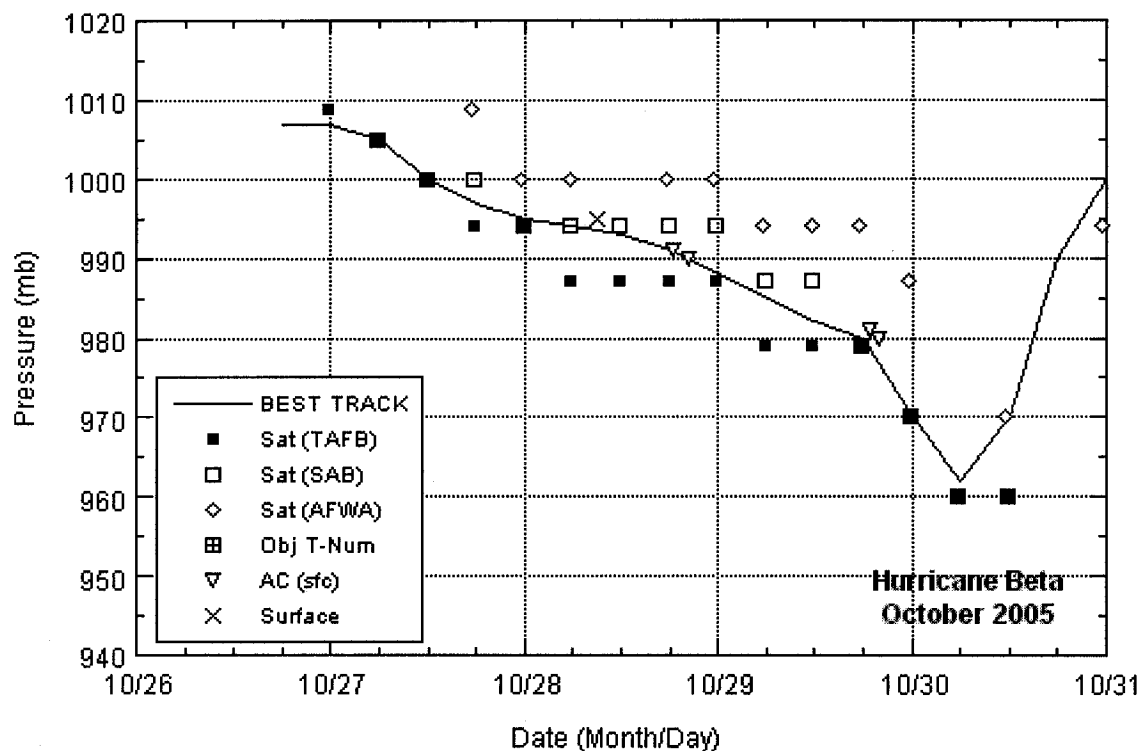


FIG. 3.2: Time series of minimum central pressure for hurricane Beta as given by the NHC best track analysis (solid line) and as estimated from various other observational platforms (symbols). (Figure courtesy of Richard Pasch.)

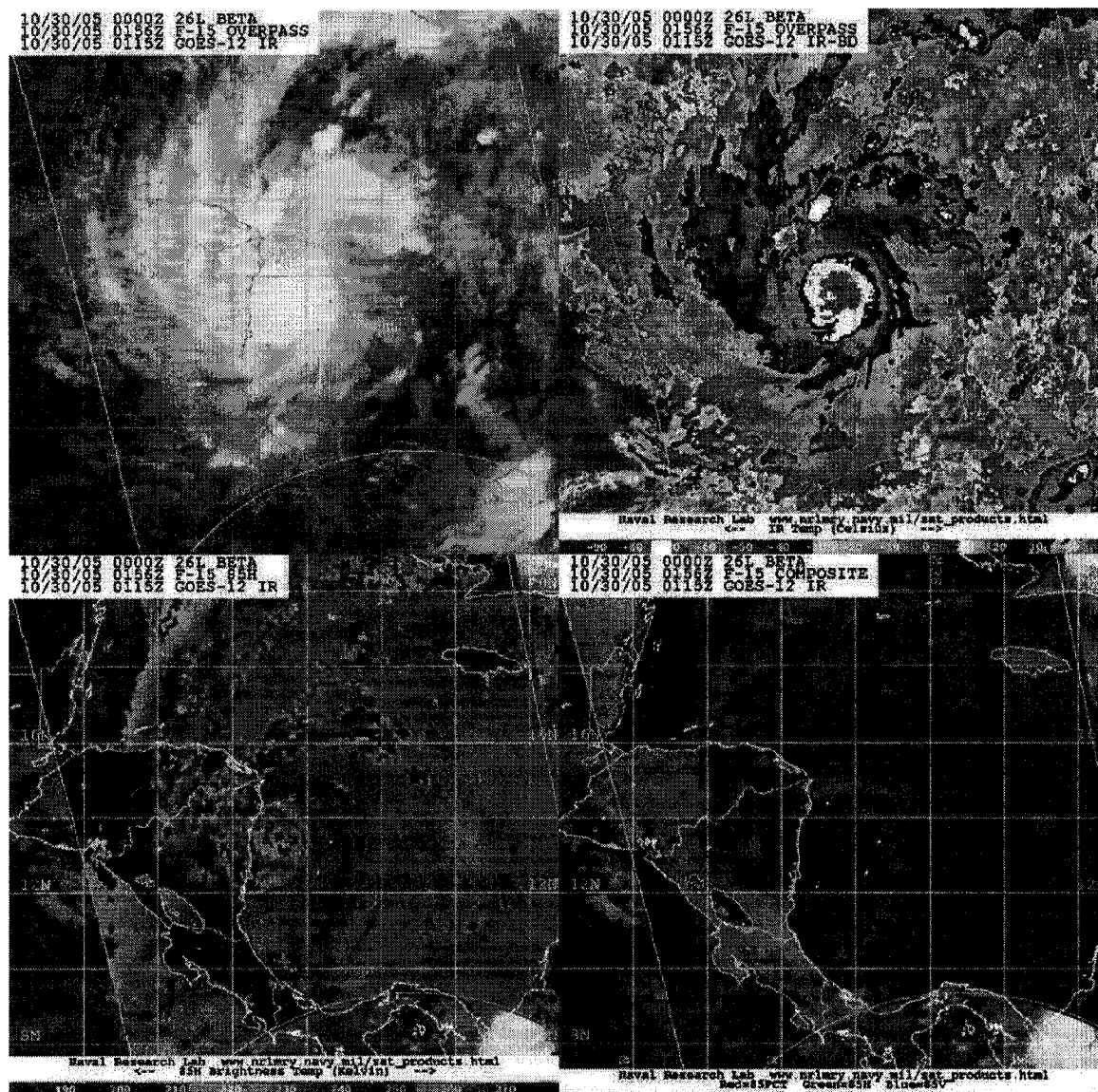


FIG. 3.3: Hurricane Beta near maximum intensity as seen by GOES infrared (upper left), GOES infrared with Dvorak enhancement (upper right), SSM/I 85 GHz horizontal polarization (lower left) and SSM/I color composite. (Image courtesy of the Naval Research Laboratory, Monterey, CA)

TABLE 3.1: NHC Forecast Error Statistics for Hurricane Beta.

Forecast	Forecast Period (h)				
	12	24	36	48	72
NHC Official Track (n mi)	27	55	74	90	88
NHC Track (1995-2004 mean) (n mi)	42	75	107	138	202
NHC Official Intensity (kt)	10	14	11	11	41
NHC Intensity (1995-2004 mean) (kt)	6	10	12	15	18

Chapter 4

Model Description and Experiment Methodology

In order to fairly and rigorously assess the potential impact of the NIS data, it is necessary to perform an observing system simulation experiment (OSSE) with a non-idealized case using a robust assimilation methodology. As discussed in the previous chapter, the case chosen is hurricane Beta from the 2005 North Atlantic hurricane season.

To do the assimilation experiments, an ensemble Kalman filter (EnKF) (Evensen, 1994) with a square-root implementation (Whitaker and Hamill, 2002, hereafter WH) will be employed. The subsequent sections provide additional detail on the model used, the simulation specifics, the OSSE methodology and the EnKF technique.

i. Model description

The University of Wisconsin Nonhydrostatic Modeling System (UW-NMS) (Tripoli, 1992) is used for all simulations described herein. The UW-NMS is a regional, quasi-compressible model phrased in a non-Boussinesq framework and is designed specifically to simulate phenomena in which scale-interaction processes are important. The UW-NMS is distinct from most other regional models in that it takes as its thermodynamic variable the ice-liquid potential temperature (Tripoli and Cotton, 1981). θ_{il} is related to the potential temperature, θ , by:

$$\theta = \theta_{il} \left(1 + \frac{L_{lv} q_{liq} + L_{il} q_{ice}}{c_p \max(T, 253)} \right), \quad (4.1)$$

where L_{lv} and L_{il} are the latent heats of condensation and fusion, respectively, q_{liq} and q_{ice} are the corresponding mixing ratios for liquid water and ice, and T is the temperature in Kelvins. In addition, the UW-NMS dynamical core is cast in an Exner function system, where the Exner function, π , is related to pressure, p , by:

$$\pi = c_p \left(\frac{p}{p_{00}} \right)^{\frac{R}{c_p}}, \quad (4.2)$$

where $R = 287 \text{ J kg}^{-1} \text{ K}^{-1}$ is the universal gas constant, $c_p = 1005 \text{ J kg}^{-1} \text{ K}^{-1}$ is the specific heat of dry air at constant pressure, and p_{00} is taken to be 100 kPa.

The other prognostic variables are the Cartesian velocity components in the zonal, meridional and vertical directions (u , v , and w , respectively), as well as the bulk mixing ratios for total water (q_T) and for each individual microphysical species being predicted (q_i).

ii. Simulation Specifics

A two-grid configuration is chosen to do the simulations, and identical configurations are employed for all simulations. An outer grid with 95 km horizontal and 500 m vertical resolution is centered at 12.5° N and 82.5° W. 85 gridpoints are used in the zonal direction and 75 in the vertical, giving the coarse grid an areal expanse of approximately 56,000 km². A second grid is deployed at the same center point and with the same vertical resolution, but with 13.6 km resolution in x and y. The dimensions of the inner nest are chosen to bound the region over which Beta executed its life cycle, and 90 gridpoints in both zonal and meridional directions prove adequate for this purpose.

Figure 4.1 shows the placement of the outer and inner nests and their relationship to the relevant geographic features. A summary of these and other details is given in table 4.1.

iii. Observing system simulation experiment (OSSE) methodology

The OSSE concept may be stated simply as an attempt to infer, by careful means, the likely impact of a proposed measurement source on a particular type of simulation (or range of simulations). Obviously, this is made problematic by the very fact of the observations' nonexistence. In order to overcome this difficulty, it is necessary to produce a simulation that serves as baseline nature or "truth." From this simulation the observations in question are generated in accord with their anticipated error characteristics and then used to produce posterior estimates (i.e. analyses) of forecasts which otherwise would differ substantially from TR. Here, these analyses are accomplished using the ensemble Kalman filter alluded to above and described in detail in section vii.

The UW-NMS configuration outlined in section ii is used to produce a truth (TR) simulation of Beta, covering the period 00Z 27 October to 12Z 30 October (of which the first 24 hours are discarded, since the model wind and precipitation fields are in the process of spinning up during this time). The initial and boundary conditions for TR are provided by GFS 1° analyses and the weekly NOAA optimum interpolation SST analysis (see table 4.1).

TR thus serves at the basis against which the assimilation experiments are assessed. In other words, the experiments described below will be evaluated on the

degree to which the observations produce analyses that are better than a control (CTL) simulation. The metrics used in defining and assessing “better” in this context are described in section vi. To be meaningful (i.e. in order not to produce artificial convergence with TR), the TR and CTL simulations should differ in a manner consistent with what we expect of the real atmosphere and a typical model simulation. There are a number of means by which this difference may be emulated (and it may even be neglected, as is the case with so-called perfect model experiments). The particular methodology used in this research is described in section iv.

Synthetic NIS observations are generated from TR as follows.

1) DOPPLER RADIAL VELOCITY

The Doppler radial velocity, V_R , observed by NIS is computed from the three velocity components (u , v , w) and terminal velocity (v_T) fields output by the model as:

$$V_R = (v_T - w) \cos \theta \cos \gamma + u \cos \theta \sin \gamma + v \sin \theta \cos \gamma, \quad (4.3)$$

where the arguments θ and γ are given by:

$$\theta = \alpha + \sin^{-1} [(d \sin \alpha)/a] \quad (4.4)$$

$$\gamma = \beta + \sin^{-1} [(d \sin \beta)/a]. \quad (4.5)$$

The arguments α and β are the scan angles in the north/south and east/west directions, respectively, given that the satellite subpoint is set at 82.5° W. The radius of the earth at the equator is a (taken as 6,378 km), and d is the range, in km, from the radar instrument to the target. Uncorrelated Gaussian random noise with a standard deviation of 0.3 m s⁻¹ is added to each observation in accordance with the anticipated instrument precision.

As is clear from equation 4.3, V_R will represent the hydrometeor fall speed only at nadir (i.e. $\alpha = \beta = \theta = \gamma = 0$).

2) EQUIVALENT REFLECTIVITY FACTOR

The synthetic NIS equivalent radar reflectivity factor, Z_e , is computed from the rain and snow mixing ratios, q_r and q_s , as well as the dry air density, ρ , and the densities of liquid water and ice, ρ_r and ρ_i , in a manner consistent with that proposed by Smith et al. (1975), Smith (1984) and Tong and Xue (2005). The contributions to the total Z_e from rain and snow are respectively:

$$Z_{er} = \frac{10^{18} \times 720 (\rho q_r)^{1.75}}{\pi^{1.75} N_r^{0.75} \rho_r^{1.75}}, \quad (4.6)$$

$$Z_{es} = \frac{10^{18} \times 720 K_i^2 \rho_s^{0.25} (\rho q_s)^{1.75}}{\pi^{1.75} K_r^2 N_s^{0.75} \rho_i^2}, \quad (4.7)$$

where N_r and N_s are the prescribed intercept parameters for snow and ice ($8.0 \times 10^6 \text{ m}^{-4}$ and $1.4 \times 10^6 \text{ m}^{-4}$, respectively). The total reflectivity is then given by:

$$Z_e = 10 \log_{10} \left(\frac{Z_{er} + Z_{es}}{1 \text{ mm}^6 \text{ m}^{-3}} \right). \quad (4.8)$$

Uncorrelated Gaussian random noise with standard deviation 5 dBZ is added to each observation.

The anticipated minimum detectable reflectivity signal is 5 dBZ, so observations of V_R and Z_e are saved from TR only at those grid points where Z_e meets or exceeds this threshold value (i.e. $Z_e \geq 5 \text{ dBZ}$). It must also be noted that no attempt is made here to account for differences in computed Z_e that would result from the use of Mie rather than

Rayleigh scattering approximations, nor is the temperature dependence of the dielectric constant taken into account.

Three experiments – VR, Z and VRZ – are conducted in which NIS-observed radial velocity, equivalent reflectivity factor, and both radial velocity and reflectivity factor, respectively, are assimilated using the EnKF configuration described in section vii. Observations are assimilated hourly to coincide with the temporal resolution of the NIS instrument, and the impact is interpreted in light of the reduction of experiment errors relative to the control errors. This will be elaborated upon further in section vi.

Assessment of NIS impact on the 12-hour period from 00Z to 12Z on 28 October will be examined in chapter 5. This represents what might be termed a typical "assimilation window" and will provide a gauge of the NIS instrument's potential to provide observations that improve the analysis of a typical tropical cyclone in a NWP model of roughly operational resolution. The degree to which this improvement in analysis leads to an improvement in forecast results is an important issue and will be explored in a chapter 6.

iv. Emulating the disparity between model and the real atmosphere

Assessment of NIS observation impact requires a control (CTL) simulation that departs from TR much as the evolution of a numerical weather prediction model departs from the evolution of the actual atmosphere. There are many ways to produce such a control, and a relatively simple approach is adopted here. A 60-member ensemble is generated by adding perturbations to the TR solution valid at 00Z 28 October (i.e. after

the 24-hour spin-up). The CTL ensemble lateral boundary conditions are perturbed about GFS forecasts initialized at 00Z on 28 October. The final boundary condition updates at 12Z on 30 October are thus 60-hour forecasts and ensure that CTL and TR diverge markedly.

Therefore, while identical computational configurations (i.e. physics and numerics) are used in both TR and CTL, the use of different boundary conditions results in separate solution trajectories for each simulation. It must be noted that, even were the initial conditions for each ensemble member exactly the same, the ensemble of boundary conditions would itself ensure that the ensemble members would, over time, diverge (from each other, and, most importantly, from TR). Clearly this violates the perfect model assumption, as can be seen by considering that for a state vector \mathbf{X} and arbitrary models M_1 and M_2 we have:

$$M_1 = M_2 \text{ iff } M_1(\mathbf{X}_t) = M_2(\mathbf{X}_t) \text{ for all } \mathbf{X}_t. \quad (4.9)$$

However, as has been noted, the simulations diverge, so that in general $M_1(\mathbf{X}_t) \neq M_2(\mathbf{X}_t)$ and hence $M_1 \neq M_2$ for any pair of simulations. Therefore, the TR and CTL models are distinct despite being numerically identical. This illustrates an important point, namely that the model must be thought of as more than a particular collection of numerical routines: it must also include the fundamental mathematical formulation of the problem to which the numerical routines provide approximate solutions. This obviously includes the set of partial differential equations that describe the relevant dynamics and thermodynamics, and the importance of the initial condition is obvious as well. Not quite

so obvious but equally important is that, for regional NWP, the model also includes the lateral boundary conditions.

The method used here thus results in a more rigorous context for the OSSE than is commonly met with in perfect model experiments (e.g. Xue et al., 2006; Wu et al., 2006), but it cannot be claimed that the degree of disparity is as great as for fully imperfect model experiments (which emphasize numerical differences). For this reason, the experiment results described in the following two chapters are termed “near-perfect” to emphasize the distinction.

v. Generation of ensemble initial (IC) and boundary conditions (BC)

As shown by Torn et al. (2006), the application of ensemble Kalman filters to regional models requires not only an ensemble of initial conditions (IC) but an ensemble of lateral boundary conditions (BC) as well. The fundamental method for generating the random fields used for both IC and BC generally follows the spectral method proposed by Evensen (2003), although there are some differences that merit mention.

The idea is to generate an ensemble of correlated pseudorandom vectors, add them to the IC (or BC), and then integrate these perturbed initial states forward with the NWP model until adjustment processes and model dynamics produce an ensemble of balanced perturbations that provide as good a representation of the essential error covariance structure as a relatively small ensemble permits. It is possible (and certainly computationally cheaper) to generate entirely uncorrelated noise, but results show (e.g. Zupanski et al., 2006) that the presence of initial correlation structure produces superior

results (i.e. better error covariance estimates), so long as some *a priori* knowledge of the correlation length scale is available.

1) ENSEMBLE INITIAL CONDITIONS

In the present case, a synoptically-informed correlation length scale of 4,000 km is chosen. N sets of perturbations are drawn from a Gaussian distribution and applied to the horizontal wind and geopotential height fields of the GFS analysis valid at 00Z 27 October. (Standard errors of $\sigma = 1 \text{ m s}^{-1}$ for u and v , and $\sigma = 10 \text{ m}$ for geopotential height are assumed.) The model is then integrated forward for 24 hours, using GFS analysis BC at 12-hour intervals, thus producing a set of N perturbations valid at 00Z 28 October:

$$\mathbf{X}'_i = \mathbf{X}_i - \overline{\mathbf{X}} ; i = 1, 2, \dots, N, \quad (4.10)$$

where the overbar denotes an average over the ensemble. These perturbations are then added to the TR simulation at 00Z 28 October to provide the appropriate IC for the N -member CTL ensemble, which in turn provides the basis for the experiments Z, VR and VRZ.

2) ENSEMBLE BOUNDARY CONDITIONS

In a similar fashion are the ensembles of BC generated. First, one must recall that the IC/BC for the TR and CTL simulations are identical through 24 hours (i.e. the spin-up phase), and both simulations use GFS analyses for their BC during this period. After this point, TR continues to use GFS analyses, and CTL uses GFS forecasts initialized at 00Z 28 October. The idea is to apply a set of N perturbations to the GFS analysis (or forecast) valid 12 hours *prior* to the time, t_{bc} , for which the BC are required (i.e. $t_i = t_{bc} - 12 \text{ h}$). The model is then integrated forward 12 hours from t_i using BC interpolated from the

appropriate GFS analysis or forecast field valid 12 hours *subsequent* to when the BC are required (i.e. $t_f = t_{bc} + 12$ h). The ensemble BC perturbations are then computed for the time midway between the valid times of the GFS files (i.e. $t = t_{bc}$) and are computed as:

$$(\mathbf{X}'_i)|_{BC} = (\mathbf{X}_i)|_{BC} - (\bar{\mathbf{X}})|_{BC}; i = 1, 2, \dots, N. \quad (4.11)$$

This allows the perturbations to evolve along the trajectory implied by the two GFS files without converging solely toward the latter. The procedure is repeated for each of the boundary update cycles (i.e. $t_{bc} = 12, 24, 36, 48$ and 60 h over the simulation period 00Z 28 October to 12Z 30 October). A schematic of the IC and BC generation scheme is provided in figure 4.2.

Two points are worth noting. First, the perturbed BC directly affect the outer grid only (at which resolution the chosen 4,000 km correlation length scale is appropriate). Second, it isn't necessary to perturb the inner grid BC directly to ensure it maintains a healthy diversity: the evolution of the perturbed outer grid provides a natural ensemble of BC to the inner nest for the duration of the simulation.

vi. Evaluation metrics

Unless otherwise stated, the term “error” will be understood to mean “root mean square error” (RMSE). The RMSE will, in general, be defined for a subset, S , of the state vector as:

$$E = \sqrt{\frac{1}{|S|} \sum_{i \in S} (\bar{\mathbf{X}}_i - \mathbf{X}_i^T)^2} \quad (4.12)$$

The overbar denotes the ensemble mean and the superscript T denotes the TR simulation. S is the subset of the state vector for which the errors are computed, and $|S|$ is simply the cardinality of S (i.e. the number of elements in S). Superscripts will be used to refer to the particular simulation in question, i.e. E^{CTL} , E^Z , E^{VR} and E^{VRZ} for the errors pertaining to CTL, Z, VR and VRZ, respectively. Furthermore, in order to more clearly demonstrate impact, E^Z , E^{VR} and E^{VRZ} will be normalized by E^{CTL} , i.e.:

$$\tilde{E}^Z = \frac{E^Z}{E^{CTL}}, \quad (4.13)$$

$$\tilde{E}^{VR} = \frac{E^{VR}}{E^{CTL}}, \quad (4.14)$$

$$\tilde{E}^{VRZ} = \frac{E^{VRZ}}{E^{CTL}}. \quad (4.15)$$

Thus, the resulting errors are expressed as a fraction of the CTL error (and not as absolute errors). This is important diagnostically, since it excludes the possibility that error reduction occurs simply as a result of CTL drifting toward TR (a possibility which has been guarded against here in any case, as mentioned in section iv.)

vii. *The ensemble Kalman filter (EnKF)*

The ensemble Kalman filter (EnKF) is a Monte Carlo implementation of the optimal linear filter (KF) developed by Kalman in 1960 (Kalman, 1960). Whereas the KF traditionally has been applied to problems in control theory, the EnKF is finding wide application as a data assimilation tool in the geosciences. Its implementation is illustrated by the following: let \mathbf{X}^f denote a column vector containing the state-space representation

of the model forecast; the analysis \mathbf{X}^a obtained by assimilating a column vector, \mathbf{Y} , of observations is:

$$\mathbf{X}^a = \mathbf{X}^f + \mathbf{K}(\mathbf{Y} - H(\mathbf{X}^f)). \quad (4.16)$$

H is a measurement operator, possibly nonlinear, which relates the state variables to the observations \mathbf{Y} , and the matrix \mathbf{K} is known as the Kalman gain. In the context of processing a single observation, \mathbf{K} provides the means for converting the discrepancy between model and observation (in observation space) at a particular point into a smooth increment applied to the entire state vector (i.e. in the state space). In practice, we won't be updating a single state vector but rather N different state vectors (which together constitute an ensemble of size N). \mathbf{K} may be defined as:

$$\mathbf{K} = \mathbf{P}\mathbf{H}^T(\mathbf{H}\mathbf{P}\mathbf{H}^T + \mathbf{R})^{-1}, \quad (4.17)$$

where the matrix products $\mathbf{P}\mathbf{H}^T$ and $\mathbf{H}\mathbf{P}\mathbf{H}^T$ can be written as (Houtekamer and Mitchell, 1998):

$$\mathbf{P}\mathbf{H}^T = \frac{1}{N-1} \sum_{i=1}^N (\mathbf{X}_i^f - \overline{\mathbf{X}^f})(H(\mathbf{X}_i^f) - \overline{H(\mathbf{X}^f)})^T, \quad (4.18)$$

$$\mathbf{H}\mathbf{P}\mathbf{H}^T = \frac{1}{N-1} \sum_{i=1}^N (H(\mathbf{X}_i^f) - \overline{H(\mathbf{X}^f)})(H(\mathbf{X}_i^f) - \overline{H(\mathbf{X}^f)})^T. \quad (4.19)$$

\mathbf{P} represents the error covariance matrix of the model forecast \mathbf{X}^f , \mathbf{R} is the observation error covariance matrix (diagonal in the present case, with error variances consistent with the NIS specifications: $0.09 \text{ m}^2\text{s}^{-2}$ for V_R , 25 dBZ^2 for Z_e), and overbars denote averages taken over the ensemble. The measurement operators, $H(\)$, are, in the present context, given explicitly by equations 4.3 and 4.8 (for radial velocity, V_R , and equivalent

reflectivity factor, Z_e , respectively). Also, care must be taken to note that subscripts in equation 4.18 refer to ensemble members (i.e. i ranges from 1 to N over the ensemble) and not to elements of a single state vector (as in equation 4.12).

Implementation of the EnKF thus requires that an initial ensemble of model states be defined, usually by perturbing a best-guess estimate of the initial state in a manner as described in section v above. Then, each ensemble member is integrated forward until observations become available, at which point equations 4.18 and 4.19 are used to calculate the products \mathbf{PH}^T and \mathbf{HPH}^T . The Kalman gain \mathbf{K} is then computed from equation 4.17, and the analysis for each ensemble member may then be computed from equation 4.16. The result is an ensemble of N analyses which are then integrated forward to the next assimilation cycle. The minimum variance estimate of \mathbf{X} is obtained at any forecast or analysis step simply by obtaining the ensemble mean.

The algorithm above forms the basis for that used in this study. However, several additional details concerning the precise formulation need to be mentioned. First, a compact covariance localization scheme with local support (Gaspari and Cohn, 1999) is used to reduce the influence of distant, noisy covariance estimates owing to the finite-sized ensemble; in this case, only those elements of the covariance field lying within 90 km of the observation point are allowed to influence the analysis. In a further effort to improve the optimality of the filter, both a square-root analysis scheme and a covariance inflation scheme as described in WH are employed. An inflation factor of 9% seems to produce the best results in conjunction with the chosen localization radius. Finally, since \mathbf{R} is assumed diagonal (i.e. observation errors are assumed to be uncorrelated)

observations are assimilated one at a time, allowing the analysis field resulting from the assimilation of one observation to become the forecast field for the next, and so on until all observations for a particular time period are assimilated (Anderson and Moore, 1979). This so-called serial approach allows the analysis scheme to be localized, meaning only that portion of the state vector lying within the localization radius is updated. This results in a significant increase in computational efficiency, since each local state vector has $O(10^3)$ elements (compared to $O(10^6)$ for the full state vector).

Finally, before the experiment results are presented, it will be noted that the analyses are obtained for the inner nest only. The reasoning here is largely practical. The NIS field of view extends only marginally beyond the poleward limit of the inner nest, meaning that a considerable computational expense would be incurred for relatively little benefit were equation 4.16 to be employed on the outer grid as well. Since two-way nesting is used in these simulations, the analysis impact in the inner grid gradually feeds up to the outer grid over the 12-hour analysis window, allowing the NIS observations to impact the environment outside the inner nest in a manner not anticipated to be greatly different than if a full, two-grid analysis were obtained.

TABLE 4.1: Relevant simulation details for TR, CTL and the experiments Z, VR, and VRZ. Boundary conditions for CTL and the experiments are perturbed about GFS forecasts initialized at 00Z 28 October.

Simulation	Resolution and timestep	Period Simulated	Initial and Boundary Conditions	Assimilation Frequency
TR	95 km / 13.6 km 360s / 45s	00Z 28 Oct – 12Z 30 Oct	IC/BC: GFS 1° Analyses	n/a
CTL	Same as TR	Same as TR	IC: GFS Analysis BC: GFS Forecasts initialized at 00Z 28 October.	n/a
VR,Z,VRZ	Same as TR	00Z 28 Oct – 12Z 28 Oct	Same as CTL.	hourly beginning at 00Z 28 Oct

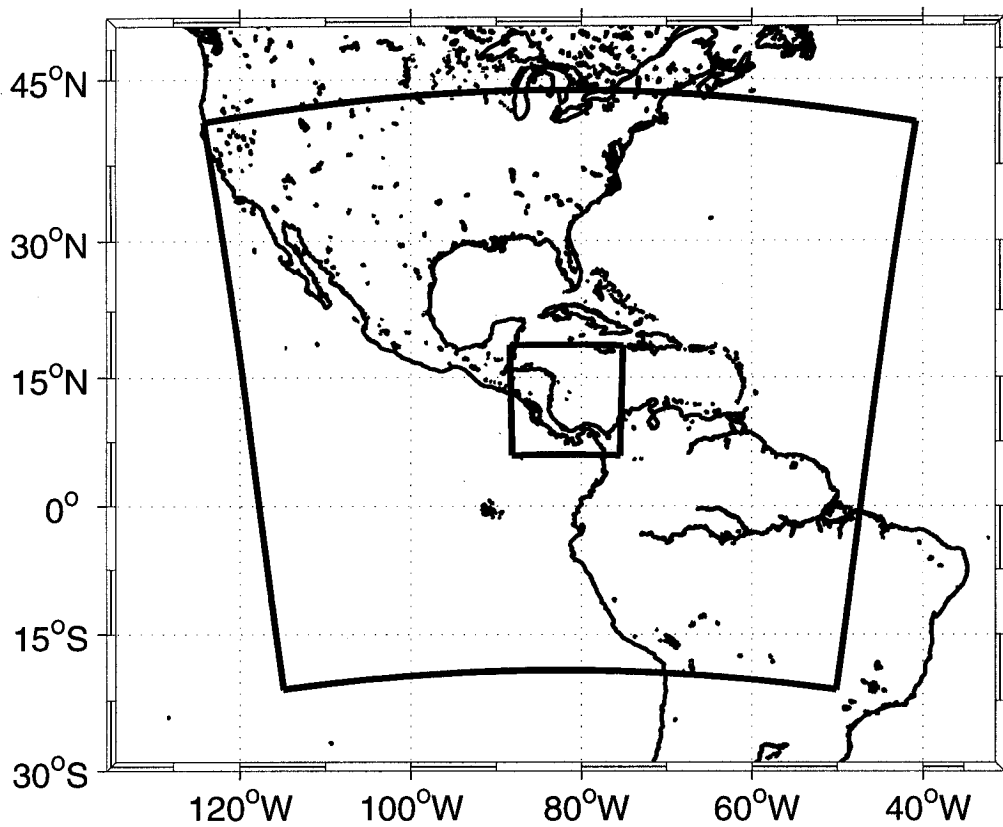
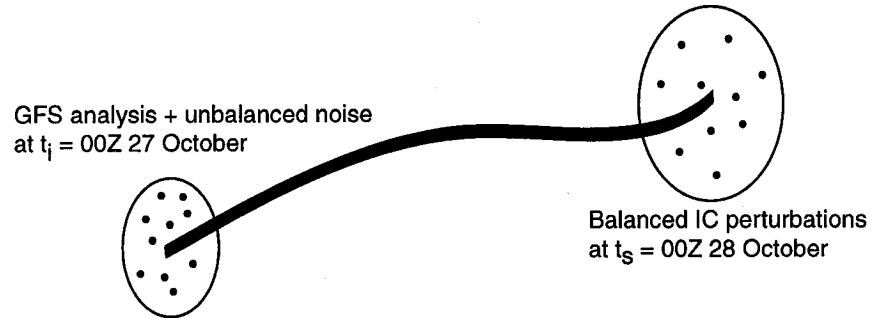


FIG. 4.1: Grid configuration for the UW-NMS simulations. The outer grid has a horizontal resolution of 95 km and the inner grid has a resolution of 13.6 km. Both grids employ 500 m resolution in the vertical.

a) Generation of Initial Conditions (IC) for $t = t_s$



b) Generation of Boundary Conditions (BC) for $t = t_{bc}$

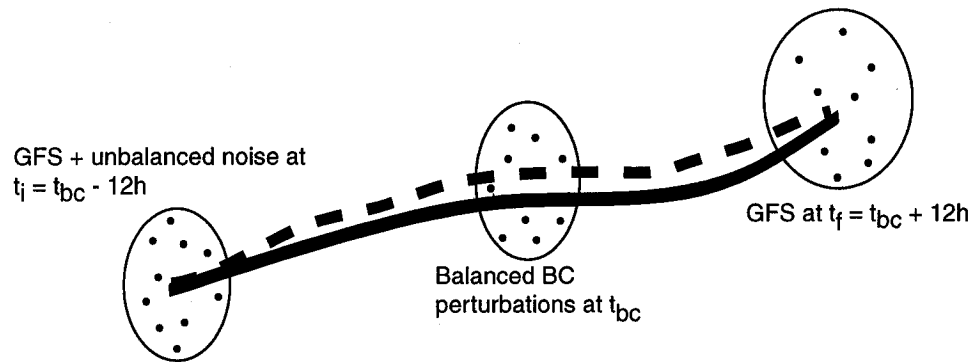


FIG. 4.2: Schematic describing the generation of (a) initial (IC) and (b) boundary conditions (BC) for the control (CTL) and experiment (VR, Z and VRZ) runs. In both panels, the dark bold curve represents the trajectory of TR, and the dashed line represents the trajectory of CTL.

Chapter 5

Analysis Impact

For the purposes of this chapter, the word analysis may have one of two meanings. First, it is used as in previous chapters to refer to an estimate of the state vector conditioned on the measured value of an observation. As before we let \mathbf{X}^f represent a model forecast, and then if an observation \mathbf{y} is made, the analysis \mathbf{X}^a is:

$$\mathbf{X}^a \sim \mathbf{X}^f \mid \mathbf{Y} = \mathbf{y}. \quad (5.1)$$

In this sense it is differentiated from the forecast valid at the same time. An equivalent terminology is *a priori* estimate (for the forecast) and *a posteriori* estimate (for the analysis).

The second sense in which analysis will be used is in reference to the model fields at the initial time (i.e. the model initial condition). In the results that follow, a 12-hour assimilation window is assumed, so 12 analyses (in the first sense) will be obtained, each at hourly intervals, and the result of these is an analysis (in the second sense) that can (and will in chapter 6) be used to initiate a model forecast.

i. Track and intensity

A long-standing tradition in tropical cyclone observation and forecasting holds that the track (usually defined as the trajectory of the sea-level pressure minimum, but other definitions are possible) and the intensity of the storm (usually defined as the maximum sustained wind, itself subject to multiple definitions) are appropriate metrics

for both describing an ongoing event as well as evaluating the skill of forecasts after the fact (e.g. Bender et al., 1992). However, tropical cyclones are large, quite often asymmetric entities, and as such very difficult to characterize solely by a center position and maximum wind value. Indeed, one can easily imagine tropical cyclones with identical tracks and intensity time series but with markedly different impacts on account of differences in size, convective asymmetry, etc. Despite its shortcomings, the track / intensity paradigm does have a legacy, and so examination of the experiment results from this perspective is undertaken first. Here, however, minimum sea-level pressure will be substituted for maximum sustained wind since it represents a more stable metric.

Figure 5.1a shows the track of Beta as simulated in TR (dark solid line) as well as the tracks of the CTL ensemble members (thin solid lines) and the CTL ensemble mean (thick dashed line) over the 12-hour assimilation window (corresponding to 00Z 28 October to 12Z 28 October). As one might expect, the small error in initial position (~10 km) grows substantially (~70km) over the 12-hour period. It is also worth noting that in 12 hours the TR position is no longer centered within the cluster of ensemble member positions, although it is still bounded by them. Figures 5.1b, 5.1c and 5.1d show the results of the Z, VR and VRZ experiments respectively. The impact of the observations in each case is obvious, as the ensemble members converge about the TR track, with the result that the ensemble mean tracks (thick dashed lines) also converge about that of the TR simulation.

Similar results hold for the intensity, as the time series of sea-level pressure show. In figure 5.2a one can see that the CTL ensemble members capture the TR state fairly

well at $t = 0\text{h}$, even slightly overestimating the intensity. However, at $t = 12\text{h}$, it is clear that the ensemble mean is drifting away from TR, underestimating the intensity at that time by 4 hPa. The impact of assimilating Z_e (figure 5.2b) and V_R (figure 5.2c) is to bring about better estimates, but in both cases the ensemble is clustered about a minimum pressure that is still 1 hPa too high. The results for assimilating both Z_e and V_R (figure 5.2d) are much better, with an ensemble mean pressure that essentially converges to TR within 6 hours and stays there, with the individual ensemble members more or less evenly distributed about TR at $t = 12\text{ h}$.

ii. Surface fields

As mentioned previously, the track and intensity alone give a rather incomplete accounting of the storm structure. To gain a better comparison amongst CTL and the three impact experiments, a sequence of snapshots of surface fields will be presented. Figure 5.3 shows surface pressure (thin solid lines, contoured every 5 hPa with the outer closed isobar being 1005 hPa) and wind speed (contours shaded every 5 kt above 34 kt, therefore showing the extent of winds in excess of tropical storm) for TR (first row), CTL (second row), Z (third row), VR (fourth row) and VRZ (fifth row) at $t = 0\text{h}$ (first column), $t = 6\text{h}$ (second column) and $t = 12\text{h}$ (third column). At the initial time, TR shows a minimal tropical storm with a pressure of 1002.5 hPa, but over the ensuing 12 hours it intensifies into a strong tropical storm, with a minimum pressure of 988 hPa and a wide swath of tropical storm and near hurricane force winds (it is worth noting that this rate of intensification is not in accord with that shown in figure 3.2). This same trend is

generally shown in the CTL ensemble mean, albeit much more conservatively. At $t = 12\text{h}$, the CTL simulation shown in figure 7f depicts a much broader circulation with no evolving inner core (as is evident in figure 5.3c).

Each of Z, VR and VRZ demonstrates a strong positive impact, with the ensemble means shown in figures 5.3i, 5.3l and 5.3o, respectively, bearing a much closer resemblance to TR than the CTL mean in 5.3f. Upon closer examination, however, the results for VRZ emerge as clearly superior, with the distribution of surface pressure and wind very close to that of TR. In addition, the calm area at the center of the wind field in 5.3o (i.e. the developing eye) is essentially collocated with that in 5.3c. Z (figure 5.3i) shows only a hint of this feature, while VR (figure 5.3l) has an elongated calm that is positioned somewhat too far east.

iii. Errors at observation locations

To gain a *prima facie* appreciation for the both the filter performance and observation impact, it is natural to first restrict examination of the errors to those locations most directly impacted by the observations (i.e. those locations at which observations were assimilated). This means the set S consists of all indices of the state vector for which the corresponding grid point values of $Z_e \geq 5$ dBZ. That is:

$$S = \{i \mid g(\mathbf{r}_Z, v)\}, \quad (5.2)$$

where g is the function that maps grid space to state space:

$$g(\mathbf{r}, v) = g(j, k, l, m) = (m-1)n_z n_x n_y + (l-1)n_z n_x + (k-1)n_z + j. \quad (5.3)$$

The vector \mathbf{r} contains the Cartesian triple that defines position in 3-d space, $\mathbf{r} = (j, k, l)$, where n_z , n_x and n_y are the number of gridpoints in the z , x and y directions, and v ranges from 1 to 8 over the prognostic variables. The vector \mathbf{r}_z is the subset of all \mathbf{r} for which the reflectivity threshold is satisfied:

$$\mathbf{r}_z = \{\mathbf{r} \mid Z_e(\mathbf{r}) \geq 5\text{dBZ}\}. \quad (5.4)$$

Figure 5.4 shows time series of the errors corresponding to Z (thin dashed line), VR (thin gray line) and VRZ (thick solid line) for nine selected fields. Errors for the three wind components – u , v and w – are shown in 5.4a., 5.4b. and 5.4c., respectively. Experiment Z demonstrates error reductions of 65 percent for u , 55 percent for v and 50 percent for w at the end of the assimilation window. Experiment VR achieves reductions of 75, 75 and 60 percent, while VRZ is slightly better, with reductions of 80, 80 and 70 percent, respectively. Since V_R is more directly coupled to the wind fields than is Z_e , it is not surprising that experiment VR demonstrates performance superior to Z . Moreover, since the information content of Z_e is clearly not negligible, the combined influence of both V_R and Z_e results in VRZ offering superior impact. Similar findings are noted for the relative vorticity, ζ , and divergence, δ , errors shown in 5.4d and 5.4e.

The errors related to the Exner function, shown in figure 5.4f, represent the least satisfactory aspect of the impact to be found. Both VR and VRZ show a reduction in error of about 45 percent by the end of the assimilation window, while Z is unable to provide a stable estimate of π after 8 hours. It will be remembered that the Exner function may be considered a proxy for pressure, so these results may be interpreted in light of the sensitivity of the perturbation pressure field to small scale (though coherent)

perturbations to the components of the 3-dimensional velocity field. Clearly, the covariance structures associated with VR are more representative of these processes and therefore more suited to providing accurate analyses of pressure (and therefore Exner function).

Figures 5.4g and 5.4h show the errors associated with the rain and snow mixing ratios, q_r and q_s . Both these quantities are used in computing Z_e , so one might expect Z to exhibit some advantage relative to VR here. Such an advantage is clear over the first 6 to 8 hours of the assimilation window, as error reductions relating to Z are consistently 10 to 20 percent lower than those relating to VR over this period. After 8 hours, though, the advantage disappears. This is indicative of improved representation of the storm dynamics (i.e. u , v , w , ζ , δ) ultimately resulting in improved representation of its microphysics. In other words, as the dynamical aspects of the evolving cyclone are brought more in line with TR, the microphysical fields gradually adjust in a physically consistent way. Similar reasoning applies to the errors associated with the ice-liquid potential temperature, θ_{il} , as shown in 5.4i.

iv. Grid-averaged errors

A metric for the bulk impact of the observations over the observation window is the normalized error averaged over the entire inner grid, in which case the set S consists of all elements in the state vector. This provides some insight into the degree to which the observations impact the analysis not only at the observation points, but throughout the entire domain. This is an important distinction, since although one expects the benefit to

be less dramatic for locations that are not observed, evidence of positive impact is still desired.

The results for the horizontal wind components (figures 5.5a and 5.5b), for the vorticity and divergence (figure 5.5d and 5.5e), and for the Exner function (figure 5.5f), are somewhat similar to their counterparts in figure 5.4. The notable difference is that the three separate experiments are more tightly clustered about values approximately 35 percent higher (u and v), 20 percent higher (ζ and δ), and 25 percent higher (π). The results for the vertical component of the wind are even more strikingly similar, a consequence of the fact that significant vertical velocities (and significant errors) are chiefly associated with significant precipitation (and this criterion is essentially fulfilled by the errors represented in figure 5.4). Similarly, figures 5.5g and 5.5h are nearly identical to 5.4g and 5.4h, indicating that rain and snow with $Z_e \geq 5$ dBZ are responsible for most of the error in those fields.

The greatest difference between the two averaging schemes is to be found as regards the errors associated with θ_{il} . Whereas the errors averaged at the observation locations (figure 5.4i) showed immediate impact of nearly 80 percent for experiment VRZ and essentially asymptotic at that value thereafter, the impact here is quite gradual and by the end of the window finally achieves 35 percent reduction.

v. Errors at locations with significant weather

In order to refine the impact assessment to those areas of greatest meteorological importance, the errors for six select fields are computed and analyzed at those surface

locations for which “significant weather” is deemed to exist. Here, significant weather is defined as wind speed of tropical storm force or greater (i.e. ≥ 34 kt) and / or rain rate in excess of 12.5 mm h^{-1} . The fields analyzed are those which themselves are of commonly held meteorological significance: surface wind speed (V_{surf}), rain rate (r), sea-level pressure (SLP), relative vorticity (ζ), divergence (δ), and total water mixing ratio (q_T).

In the case of surface wind speed (figure 5.6a) four hours is required to converge to a solution with 80 percent reduction in error for VRZ. It takes about two hours longer for VR to achieve the same level of improvement. Z demonstrates a greater degree of instability in its estimate, which approaches 70 percent reduction after six hours only to decrease to 40 percent at nine hours before finally settling back to 70 percent at 12 hours. The results for relative vorticity (5.6d) and divergence (5.6e) are similar.

The error reduction for rain rate, shown in 5.6b, demonstrates more consistency among the three experiments, with improvements ranging from 65 (Z and VR) to 80 percent (VRZ) at 12 hours. Sea-level pressure (figure 5.6c) achieves 80 percent reduction for both VR and VRZ, while Z ranges about 10 to 15 percent higher. The results for total water mixing ratio, as shown in 5.6f, demonstrate a 60 percent reduction at 12 hours versus 40 percent for Z.

vi. Layer-averaged errors

Finally, to gain a more complete perspective on the impact of the NIS observations, the errors are averaged over each vertical level, both for the observations

alone (as in figure 5.4) and for the entire grid (as in figure 5.5). The results are shown for VRZ in figures 5.7 and 5.8, and the results are illuminating.

What one notices immediately is that for δ , π , q_r , q_s and θ_{il} , there is a tendency over the duration of the assimilation window for the observation impact to be diminished between 4 and 5 km. This corresponds to the melting layer in the model, and this consideration leads to the cause of this behavior. This region contains populations of both snow and rain, making observation-model error correlations related to Z_e more complex than in areas with a single population of condensate. In addition, as its name would imply, the melting zone is a region of transition from snow (with its near constant terminal velocity) to rain, the terminal velocity of which increases rapidly with diameter. This sharp transition results in a near discontinuity of V_R , which results in a likewise sharply demarcated covariance structure that is difficult to capture fully with a 60-member ensemble. Similar findings are noted in experiments Z and VR (not shown).

Another feature of interest can be seen in figure 5.7. It is recognized as an area of enhanced error (i.e. 10 to 30 percent greater than surrounding areas) in the u , v and w fields (figures 5.7a, 5.7b, 5.7c, respectively) between 5 and 12 km during the four to six hour period. Corresponding structures show up in the ζ and δ fields (5.7d and 5.7e), as well as in the π , q_s and θ_{il} fields. The coherence of these error structures suggests a robust physical process, and this is indeed the case. Figure 5.2 shows that TR intensified rapidly over the four hour period from $t = 4$ h to $t = 8$ h (the pressure fell 9 hPa during this time). This intensification was preceded and accompanied by a large convective burst (not shown) between $t = 4$ h and $t = 6$ h (the time frame for which the coherent error structures

were noted). This bursting / intensification phenomenon is commonly observed in tropical cyclones, and though it does result in a temporary disruption in the analysis quality at upper levels, the analysis quality in general continues to improve over the duration of the assimilation window.

Aside from that associated with the two features mentioned above, the vertical structure of the error fields is much as one might expect, with a greater degree of overall impact apparent in figure 5.7 relative to figure 5.8, which depicts the errors averaged over the entire grid rather than only at the observation locations.

vii. Conclusions

It cannot be asserted that the results presented here guarantee a corresponding level of performance in real-world application, for if there is one lesson well-learned in NWP it is that the real atmosphere-ocean system shall depart from our best efforts to simulate it in seemingly new and often surprising ways. Moreover, the OSSE experimentalist must in his or her own terms adjudge the best means of emulating the inherent misfit between nature and model. No amount of effort can effectively span the full range of possible departure, and with that in mind, the decision has been made here to force the two solutions, TR and CTL, to diverge by means of enforcing different lateral boundary conditions. There certainly are other means of eliciting such divergence, but that used here is relatively simple, effective, and provides assurance that the impact seen in the analyses is due to the information content of the observations (and the robustness

of the EnKF) rather than to unanticipated and undesirable affinity of CTL for the TR solution.

This being said, under the conditions chosen for these experiments, the impact of NIS is demonstrated to be significant over a 12-hour assimilation window. Indeed, a window period of four to six hours appears sufficient to achieve statistical convergence to analysis states which exhibit from 20 to 80 percent improvement relative to CTL when errors are computed over the entire grid. When consideration of impact is restricted to those points at which observations are made, the improvement is more homogeneous and ranges from 40 to 80 percent. When consideration is further restricted to those points at which significant weather is occurring, the impact homogenizes nearly completely, with 60 to 80 percent improvement noted for all experiments.

Broadly speaking, the Doppler radial velocity, V_R is most effective in reducing the errors related to “dynamical” fields (u , v , w , ζ , δ , π) and the equivalent reflectivity factor, Z_e , is most effective with regard to the microphysical (q_r and q_s) and thermodynamic (θ_{il}) fields. As would be expected, the results are generally superior when assimilating both V_R and Z_e (i.e. experiment VRZ). This superiority is most evident at the early stages of the assimilation cycle, when combined information content of both observation types is greater than either one separately. Later, as the cumulative impact of observations at each cycle begins to show, the estimates for VR and VRZ tend, in most cases, to converge.

An interesting feature of each of the experiments, and demonstrated herein for VRZ, is the recalcitrance of errors in the melting layer. In particular, the errors related to divergence, Exner function, rain and snow mixing ratios, and ice-liquid potential

temperature range from 10 to 50 percent higher in this region than either below or aloft. Such behavior stems from the endemic physical complexity involved in a layer of mixed-phase clouds, implying a more complex observation-model error covariance structure with regard to both V_R and Z_e . While the results shown are suboptimal in the sense that the impact of observations is less apparent (and more inert) here, the performance may be enhanced with the use of a larger ensemble that allows a fuller and more accurate representation of the correlations involved. This remains to be tested.

While the results presented here are encouraging, the true value of NIS will only be fully appreciated if its influence upon forecasts is considered. An examination of forecast impact with the case under consideration will be presented in the next chapter.

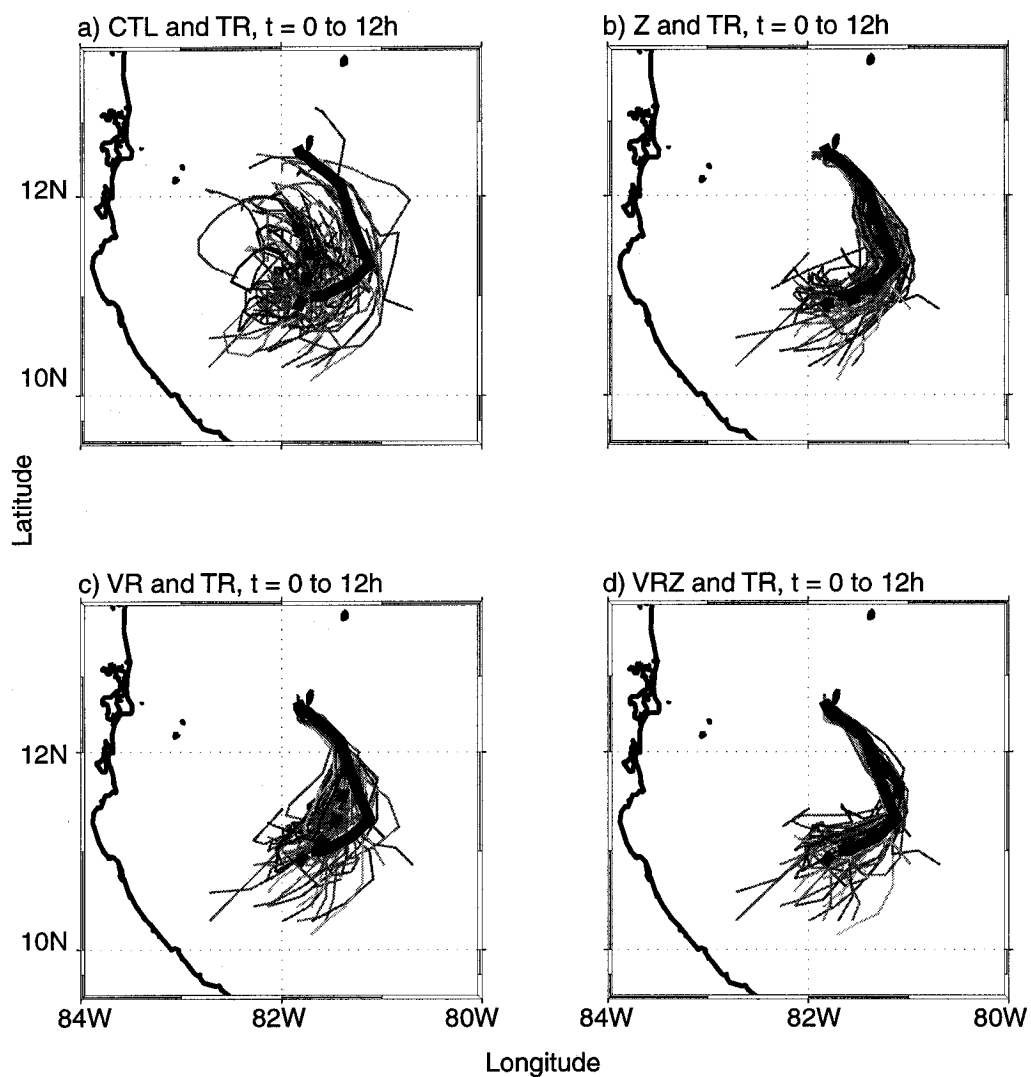


FIG. 5.1: Tracks of ensemble members (thin solid lines), ensemble means (thick dashed lines) and the TR simulation (thick solid line) over the twelve-hour period 00Z 28 October – 12Z 28 October. CTL results are shown in (a), and results for the experiments Z, VR and VRZ are shown in (b), (c) and (d) respectively.

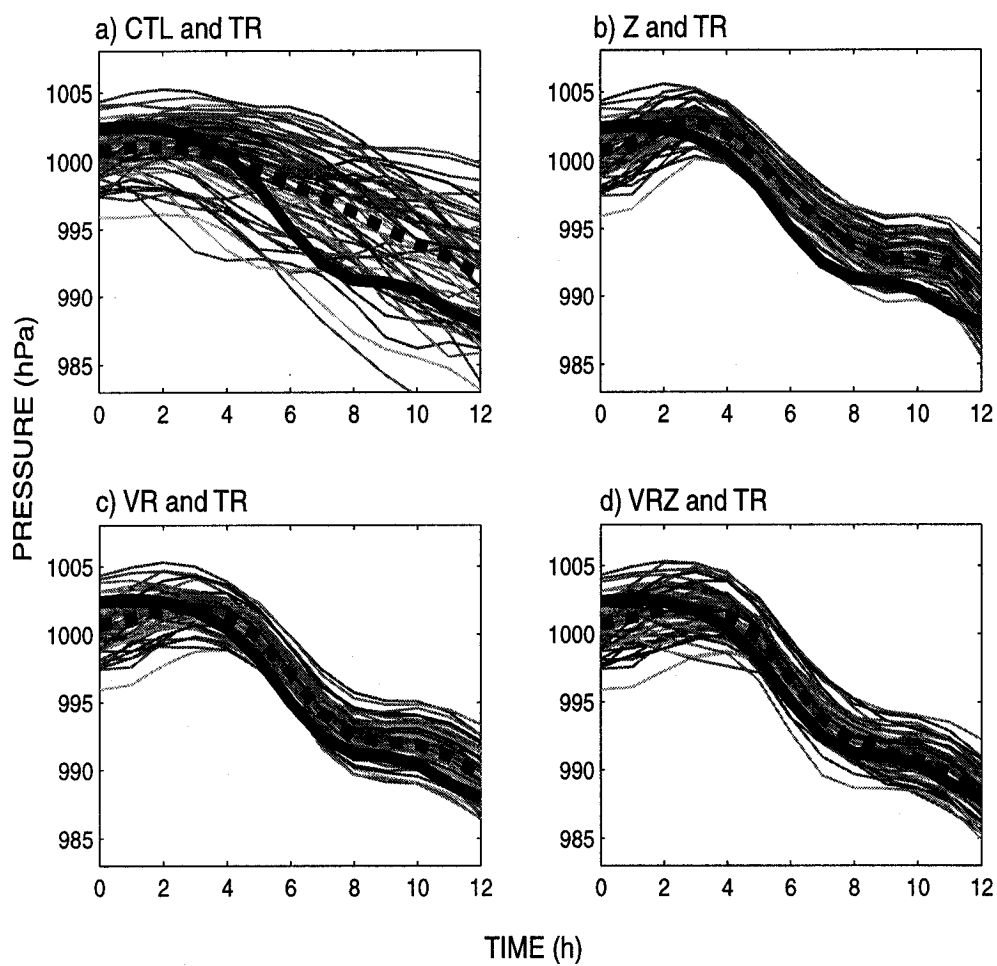


FIG. 5.2: As in figure 5.1, but for minimum sea-level pressure.

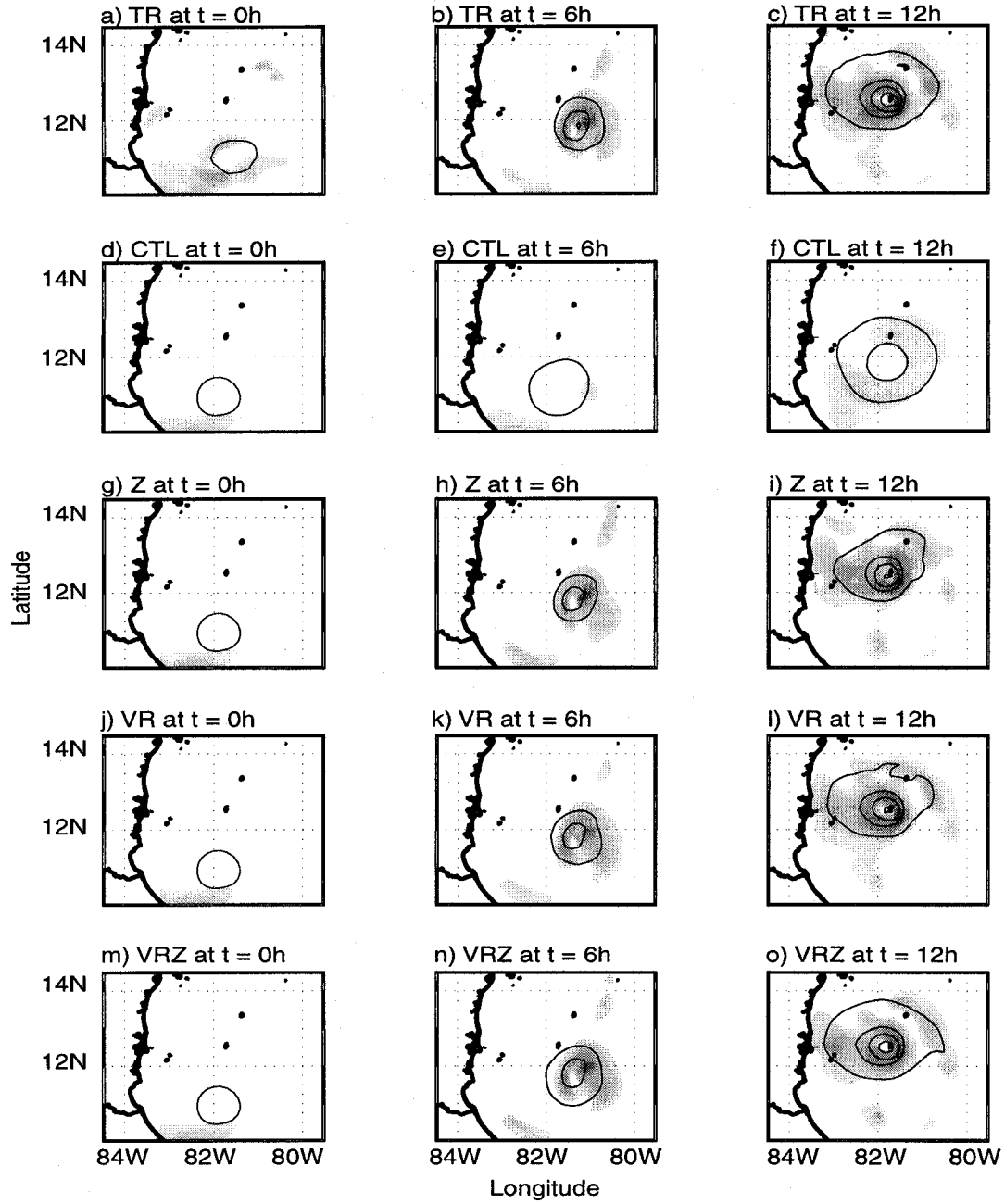


FIG. 5.3: Sea-level pressure (SLP) and surface wind speed at six-hour intervals over the assimilation window for TR, (a) – (c); CTL, (d) – (f); Z, (g) – (i); VR, (j) – (l); and VRZ, (m) – (o). SLP is contoured at 5 hPa intervals (the outer closed isobar being 1005 hPa) and wind speed values greater than 34 kt are shaded at 5 kt intervals.

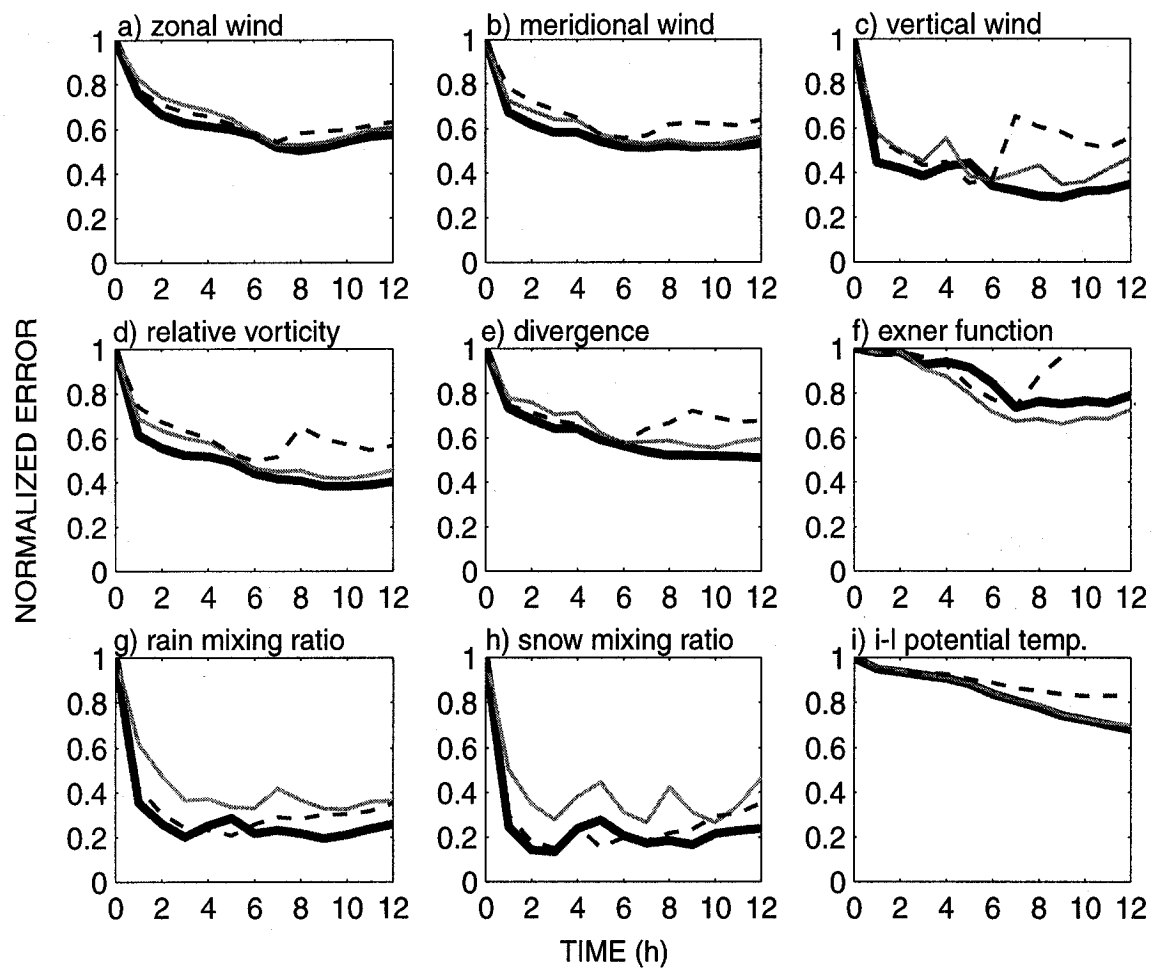


FIG. 5.4: Time series of normalized analysis RMSE over the analysis window. Errors pertaining to Z, VR and VRZ are depicted with a thin dashed line, a thin gray line, and a thick solid line, respectively. The errors are computed only at those grid points in the inner nest where the equivalent reflectivity factor, Z_e , meets or exceeds 5 dBZ (i.e. grid points at which observations have been assimilated).

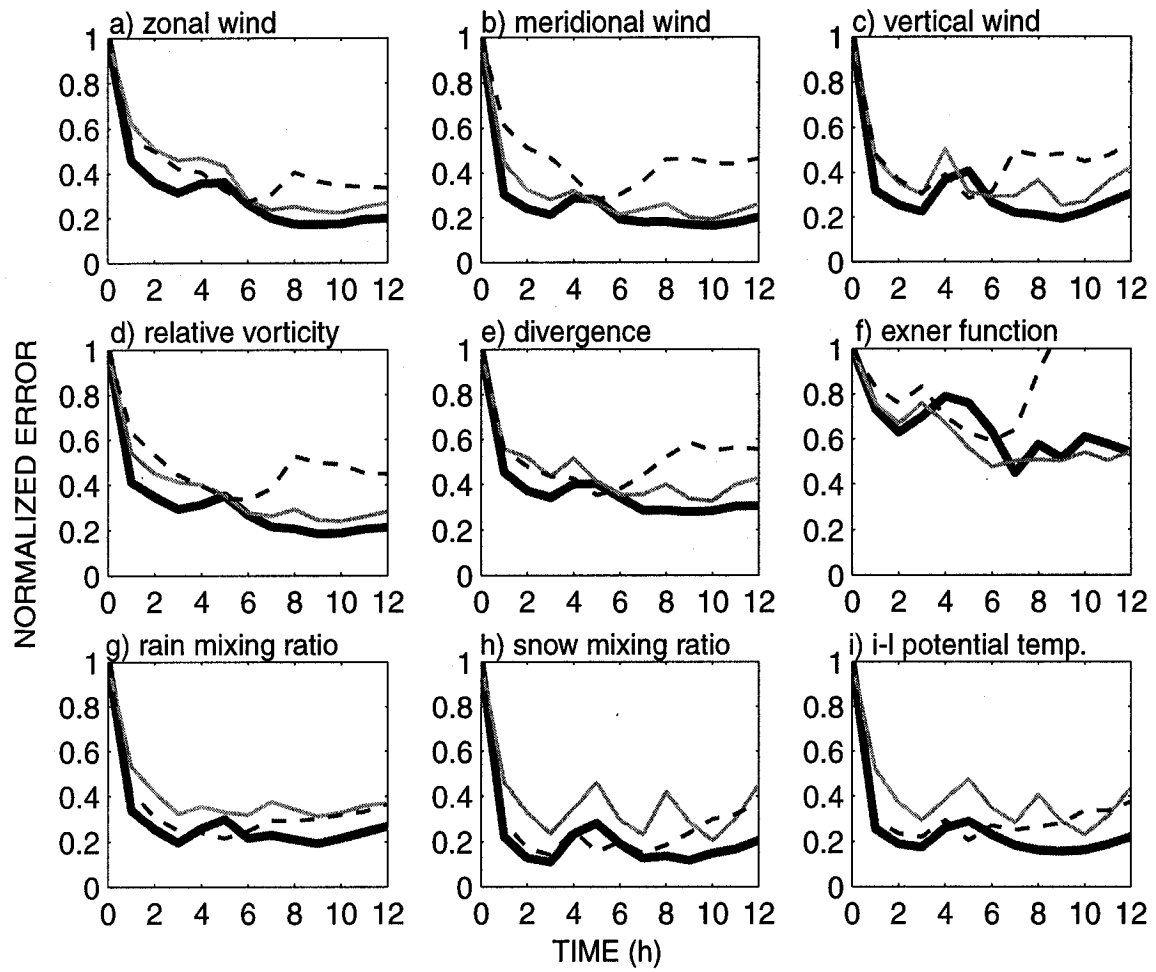


FIG. 5.5: As in figure 5.4, but the errors are computed at each grid point in the inner nest.

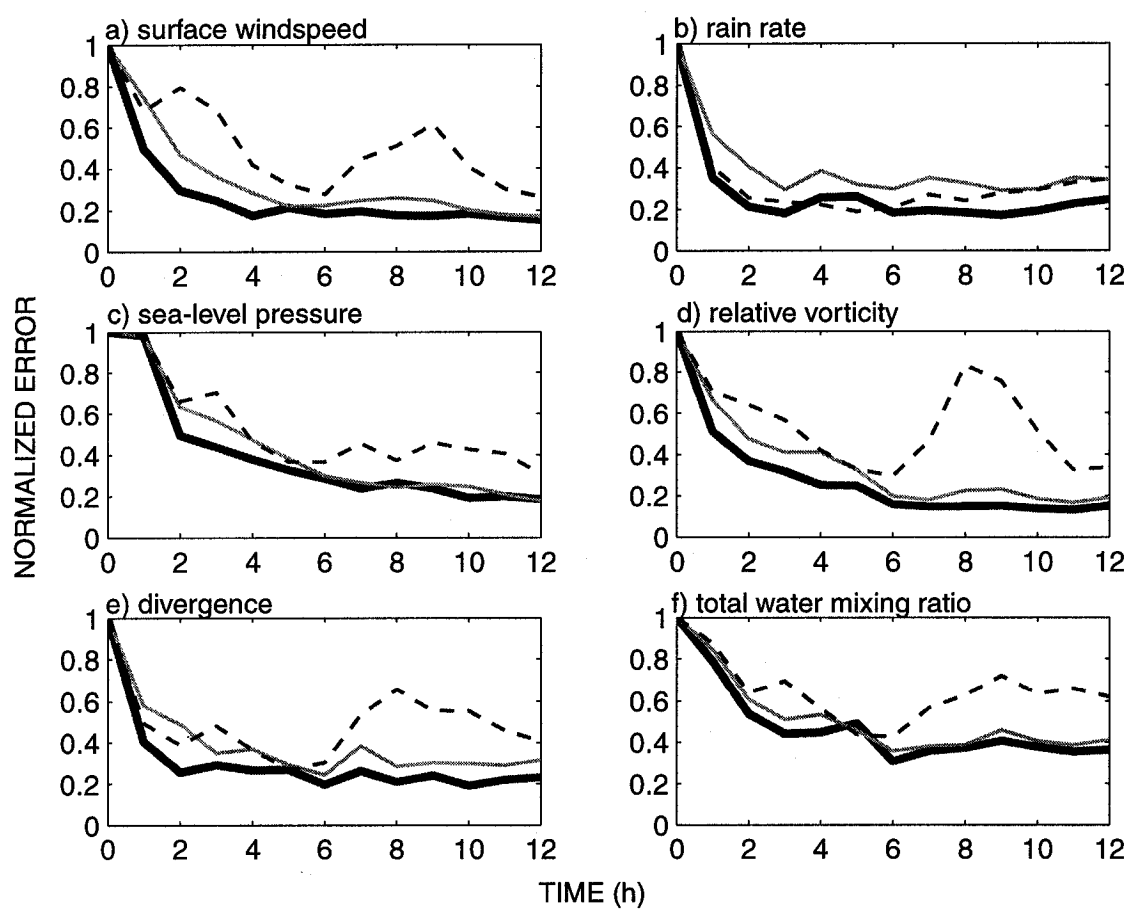


FIG. 5.6: As in figures 5.4 and 5.5, but the errors are computed only at those surface locations with significant weather (here defined as wind speed > 34 kt and/or rain rate $> 12.5 \text{ mm h}^{-1}$).

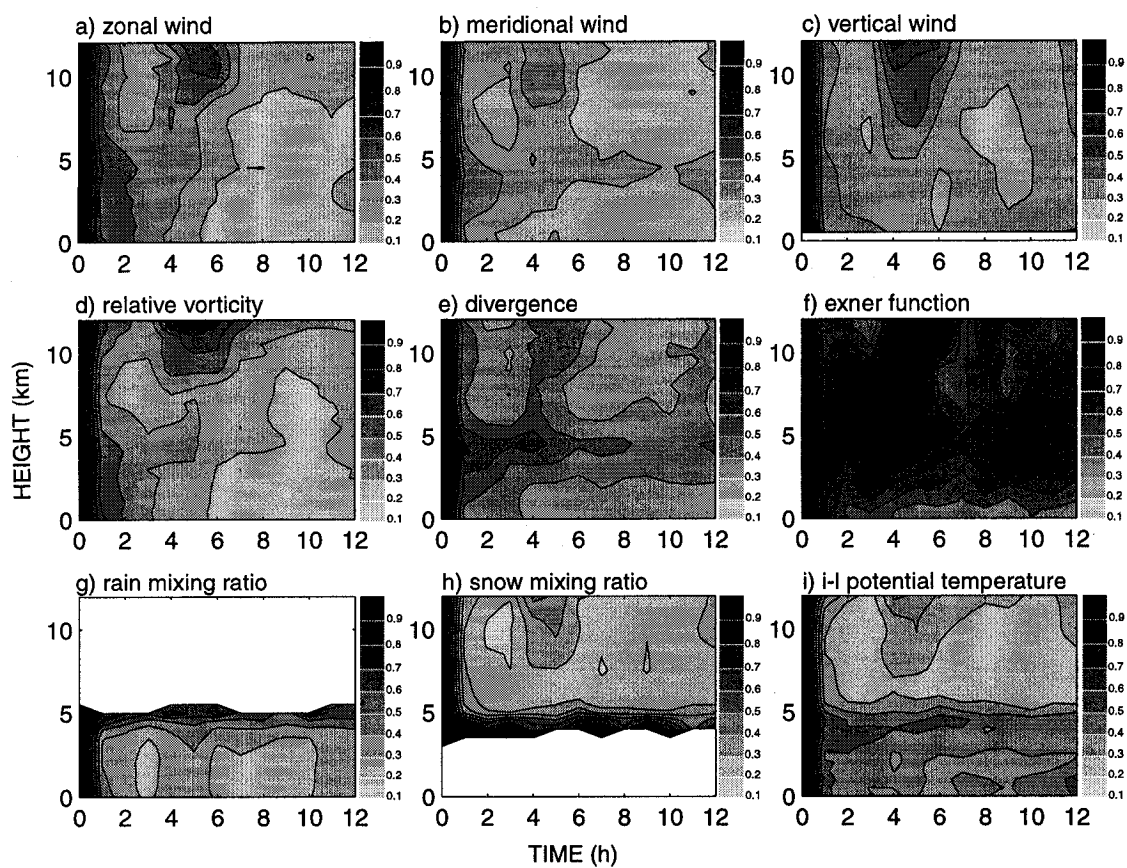


FIG. 5.7: Layer-averaged RMSE over the analysis window for experiment VRZ. As in figure 5.4, the errors are computed for those points for which $Z_e \geq 5$ dBZ.

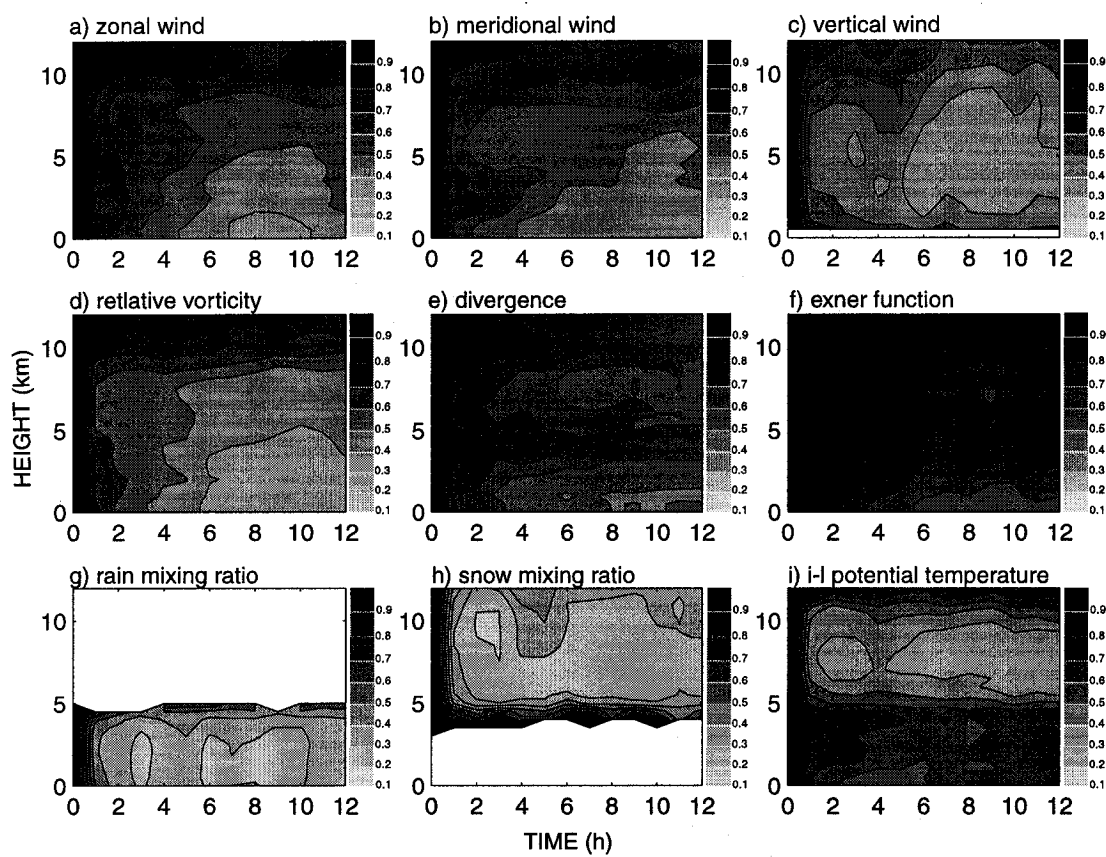


FIG. 5.8: As in figure 5.7, but the errors are computed for each point in the inner grid.

Chapter 6

Forecast Impact

In the previous chapter, results were presented which demonstrated the effectiveness of synthetic NIS observations in significantly reducing analysis errors over a 12-hour assimilation window. In this chapter, the endurance of the analysis phase impact is investigated in the context of a 48-hour ensemble forecast initiated from the 12-hour VRZ analysis described in the chapter 5.

The period from 12Z 28 October to 12Z 30 October presents several forecast challenges, the most notable of which are a transition in Beta's steering (including its westward turn toward Nicaragua, preceded by an irregular, trochoidal track with three distinct counterclockwise loops) as well as intensification to a near-major hurricane and then weakening just prior to landfall at 12Z 30 October. Figure 6.1 illustrates that the CTL ensemble forecast, while generally indicative of a west-northwestward to westward track, is unable to capture the details of Beta's motion. Similar results hold for intensity (figure 6.2), as CTL provides a poor estimate of TR minimum sea-level pressure beyond 12 (and especially beyond 24) hours. The presence of these track and intensity difficulties provides an excellent test of NIS impact, and the following three sections present an analysis thereof. The first section provides a comparison of the CTL and VRZ track and intensity errors over the forecast period. The second section presents time series of wind and rain at six relevant surface stations within the computational domain, examining the NIS impact in an operational meteorological forecast context. This context is maintained

in section three, in which the skill of the VRZ forecast is evaluated against CTL using standard methods.

i. CTL and VRZ track and intensity errors

As was shown in figures 6.1 and 6.2, the CTL ensemble forecast performs rather poorly with respect to the track and intensity (minimum sea-level pressure) metrics, especially after 24 hours. This notion is confirmed by explicitly considering the absolute track and intensity errors over the forecast period, as is shown in figure 6.3. The upper panel, 6.3a, shows track errors (in nautical miles) for each ensemble member (light gray lines) and for the ensemble mean (heavy black line). Also plotted are the 12, 24, 36 and 48-hour track errors for the official NHC forecasts issued for Beta (black dots are the average over all forecasts, and the red dots represent errors for the forecast issued at 11Z 28 October). The CTL errors are generally higher than the NHC errors during the first 24 hours, and less than the NHC errors thereafter. Figure 6.3b shows intensity errors (in knots) for the CTL forecast with a similar superimposition of the NHC intensity errors. The CTL errors match the NHC errors well through 24 hours and are somewhat higher thereafter. Hence, when taken together, the track and intensity errors related to CTL seem to convey a level of predictability similar to that conveyed by the real-time NHC forecasts for Beta and thus represent a realistic standard against which the NIS-influenced forecast (VRZ) can be judged.

The results for VRZ are shown in figure 6.4 and reveal significant improvement relative to CTL. The track errors, shown in 6.4a, increase slowly from near zero at the

initial time to near 20 n mi at 24 hours. The CTL errors, by comparison, exhibit a periodic structure related to the looping, trochoidal character of the TR track and the inability of CTL to capture this motion. By comparison, the smooth growth of the VRZ errors demonstrates that the essential nature of the TR steering is being captured. Beyond 24 hours, both CTL and VRZ show essentially linear error growth (from ~40 to ~60 n mi for CTL and from ~ 20 to ~ 60 n mi for VRZ) and the advantage enjoyed by VRZ diminishes and essentially disappears by 48 hours. Averaged over the duration of the forecast, the VRZ track errors are reduced 56 percent relative to CTL (24.1 n mi mean error for VRZ vs. 55.2 n mi for CTL).

The results for intensity are somewhat different. The CTL intensity errors are steady at just more than 5 kt over the first 24 hours, and the VRZ results are similarly steady though some 1 or 2 knots smaller. Over the ensuing 24 hours, however, the CTL errors begin to increase at roughly 1 kt per hour, reaching near 30 kt at 48 hours, whereas the VRZ errors remain steady through 36 hours. Thereafter, a similar 1 kt per hour rate of increase is noted and at the final time the VRZ intensity error is 13 kt, less than half that of CTL. This represents an intensity error reduction of 65 percent when averaged over the 48-hour period (4.6 kt for VRZ vs. 13.2 kt for CTL). The VRZ track and intensity forecasts are summarized in figures 6.5 and 6.6 (which may be directly compared to similar plots for CTL in figures 6.1 and 6.2).

ii. Time series of surface wind and rain at 6 stations

While the errors of center position and maximum sustained wind (and the reduction thereof in the VRZ forecast) are a good indicator of performance, for considerations relating to practical forecasting, it is perhaps more illuminating to consider the errors at specific locations (locations for which forecasts would need to be made, and warnings issued, in a real operational setting). To do so, six stations (figure 6.7) are chosen as being representative of different aspects of the forecast problem. Station 1 is Rio Blanco, Nicaragua, a station well-inland and thus disqualified from storm-surge or extreme wind impacts. Station 1 represents the type location in Central America often threatened by TC-induced fresh water flooding. The remaining Stations are on the open coast: 2 is Puerto Cabezas, Nicaragua (just north of the TR landfall point and on that account would be expected to receive significant wind and rain impact); 3 is San Andres Island (which the center of TR passed near at forecast hour 12) ; 4 is the landfall point for TR; 5 is Puerto Limon, Costa Rica (far removed from any anticipated impact) and finally 6 is Puerto Lempira, Honduras (over which several significant convective bands passed in the latter half of the forecast period).

Time series of wind and rain rate are shown for each of the above stations in figure 6.8 (values for TR are shown in black, values for CTL are shown in red, and values for VRZ are shown in green). The most striking aspect of the results is that VRZ surface wind is seen to agree nearly perfectly with TR at all locations over the first 12 to 24 hours, indicative of continued strong analysis impact, with some degree of smoothing and dispersion thereafter. This is borne out by the time series correlations summarized in

table 6.1. VRZ surface wind aggregated across the 6 stations correlates with the TR surface wind at $r = 0.9355$ over the first 24 hours and at $r = 0.8481$ over the second 24 hours, while CTL correlates at $r = 0.6848$ and $r = 0.4518$, respectively. For both time intervals, the difference in correlation, Δr , between VRZ and CTL is statistically significant at the .01 level as determined using Fisher's r-z transformation and corresponding z-test (Blalock, 1972). Clearly then the 12-hour NIS assimilation cycle leads to a strong impact on surface wind forecasts through 48 hours.

The results are somewhat less convincing for rain rate. As seen in table 6.1, the first 24 hours indicate a statistically significant difference in correlation between the CTL and VRZ forecasts (0.2805 vs. 0.7133, respectively), but this significance disappears over the final 24 hours of the forecast (0.4332 vs. 0.5051, respectively). Typical of the reason for this loss of impact is the inability of VRZ to resolve significant convective rain events on the cyclone's periphery later in the period (see, e.g., fig. 6.8b or 6.8f).

iii. Forecast skill

The foregoing two sections provide quantitative evidence of positive NIS impact on forecasts of surface wind and rain rate, but in so doing use metrics that are either standard but somewhat vague (section i) or quite specific if non-standard (section ii). In this section, the Brier (BS) and Brier skill scores (BSS) (Brier, 1950) will be computed for the forecasts in order to place the results in more familiar, conventional terms that, it is hoped, strike an adequate balance between the standard and specific.

The Brier skill score for forecast VRZ is defined as:

$$BSS_{VRZ} = 1 - \frac{BS_{VRZ}}{BS_{CTL}}, \quad (6.1)$$

where the Brier score, BS, is:

$$BS = \frac{1}{|S|} \sum_{k \in S} (f_k - o_k)^2. \quad (6.2)$$

As before, S is the subset of the state space for which the forecast is being evaluated, and f and o are the probabilities of an event occurring in the forecast and in TR, respectively. The o_k are binary random variables that take the value 0 if a certain threshold is not exceeded and 1 if the threshold is exceeded. The f_k are the probabilities of threshold exceedance as determined from the ensemble forecast. For example, if 39 of 60 members exceed the threshold at some point k , then $f_k = 39/60 = 0.65$. If $o_k = 1$, then the resulting Brier score is $BS = (0.65 - 1)^2 = 0.1225$. The Brier score is, as evident from 6.2, analogous to mean-squared error (MSE) with the difference being that errors in probability of exceedance (rather than in actual physical quantities) are being measured. As with MSE, the lower the value of the BS, the higher degree of performance implied. The Brier skill score, BSS, on the other hand, is a measure of skill relative to some reference. Here that reference is taken to be CTL, and the resulting BSS is thus a measure of the percent improvement relative to CTL (and is thus analogous to the relative error metrics used in chapter 5).

Six threshold criteria – three pertaining to wind and three to rain – are chosen in order to evaluate different aspects of the forecast. The threshold wind values are 34 kt (tropical storm force), 64 kt (hurricane force) and 84 kt (corresponding to category 2

hurricane). The threshold rain rate values are 0 mm h^{-1} (to differentiate grid points with and without rain), 12.5 mm h^{-1} (moderate rain) and 25 mm h^{-1} (heavy rain). These thresholds are summarized in table 6.2, and figure 6.9 shows plotted values of BSS_{VRZ} for each threshold over the 48-hour forecast period.

Looking first at the results for the surface wind, it is clear that the VRZ forecast offers broad 50 to 60 percent improvement over CTL for the duration of the forecast with regard to forecasting tropical-storm-force winds ($w1$). A similar degree of improvement is noted for hurricane-force winds ($w2$) over the first 24 hours, but thence a steady decline begins and by the end of the forecast the improvement is only 10 percent. Results for category 2 threshold winds ($w3$) are about 25 percent improvement over the first 24 hours followed by a steady decline as in $w2$, with the end result that by the end of the forecast period there is essentially no difference between VRZ and CTL.

The results for rain are somewhat more homogeneous and generally support the results presented in section ii (i.e. that rain is more difficult to forecast than surface wind). The skill related to each threshold value is initially in excess of 65 percent but quickly drops to 30 percent or less only 5 hours into the forecast. Thereafter the VRZ forecast's ability to distinguish rainy from non-rainy grid points ($r1$) remains essentially steady at 30 percent better than CTL. The performance for moderate rain ($r2$) and heavy rain ($r3$) is generally poorer, decreasing to just greater than 0 at 12 hours and remaining there (with one small impulse of skill near 16 hours) until becoming indistinguishable from CTL at 43 hours.

iv. Conclusions

The results presented demonstrate that the impact achieved in the analysis phase does indeed translate into the forecast phase. When the errors relating to track are considered, the greatest improvement occurs during the first 24 hours, with a gradual diminution of impact thereafter. With respect to intensity, the greatest relative impact is noted over the final 24 hours, a large measure of which is due to the fact that the VRZ hurricane makes landfall near 06Z 30 October (rather than 00Z 30 October, as in CTL), which results in a delayed weakening more in line with the TR simulation. This result is notable in that it highlights the potential interdependence of track and intensity forecasts in general.

When the results are considered for 6 typical surface stations, it is seen that the VRZ wind forecast remains distinctly better than CTL for the duration of the forecast, demonstrating significant correlation with the TR time series at the aggregate of the stations. The VRZ rain forecast performs quite well relative to CTL over the first 24 hours, but this advantage essentially disappears over the final 24 hours of the forecast. An examination of the particular time series reveals that this loss of impact results from an inability of VRZ to track heavy rain events later in the forecast, especially at locations distant from the storm center. Also evident from the station plots is that after 18 to 24 hours, the impact of increasing ensemble spread is manifest as a smoother time series for both wind and rain.

To determine whether the results presented for the selected surface stations are in accord with the performance over the entire grid, and also to place the results in a more

familiar, probabilistic context, the Brier skill scores (BSS) are computed for the VRZ forecasts of surface wind and rain rate. The BSS generally support the results of the first two sections, showing that VRZ demonstrates a substantially greater degree of skill with wind forecasts than with rain, especially beyond 24 hours. It is additionally shown that skill for wind forecasts depends on the particular threshold wind speed, with greater skill for forecasts of tropical storm force winds (>34 kt) than for hurricane force or higher winds (>64 kt). The sensitivity of the BSS to the chosen threshold highlights the importance of not placing undue emphasis on grid-averaged error metrics (such as RMSE). To put it another way, weather occurs at specific locations at specific times, and it is precisely this sort of detail that must be properly represented to achieve improved forecasts.

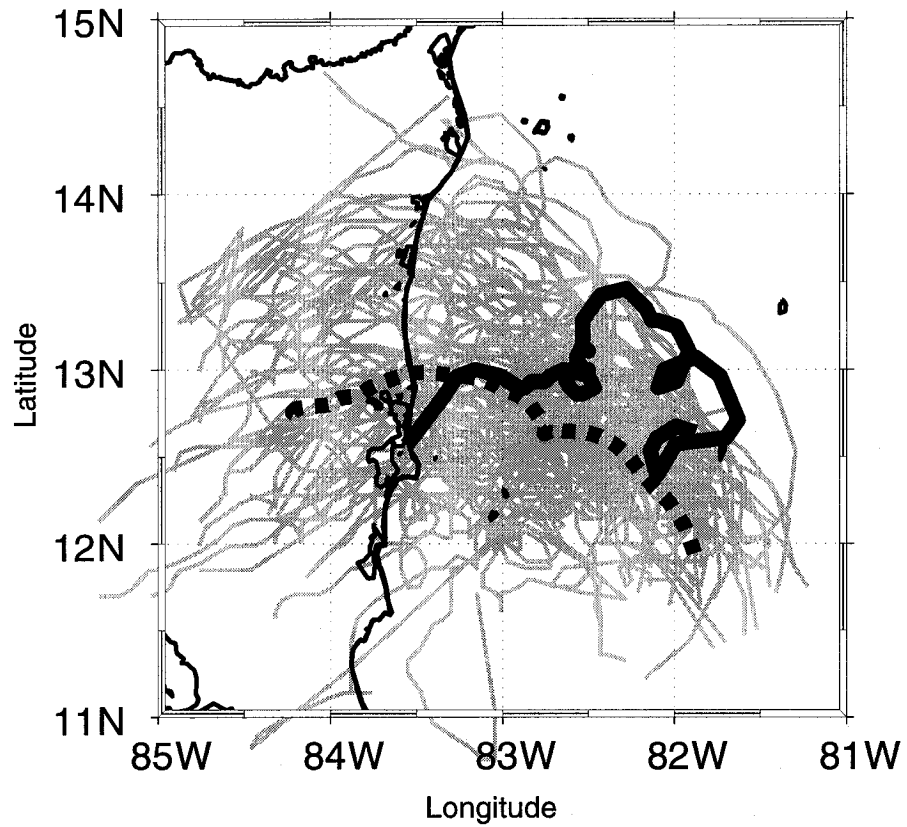


FIG. 6.1: Comparison of the TR track and the CTL forecast for the period 12Z 28 October to 12Z 30 October. TR is the heavy line, individual ensemble members are represented by thin gray lines, and the ensemble mean by the heavy dashed line).

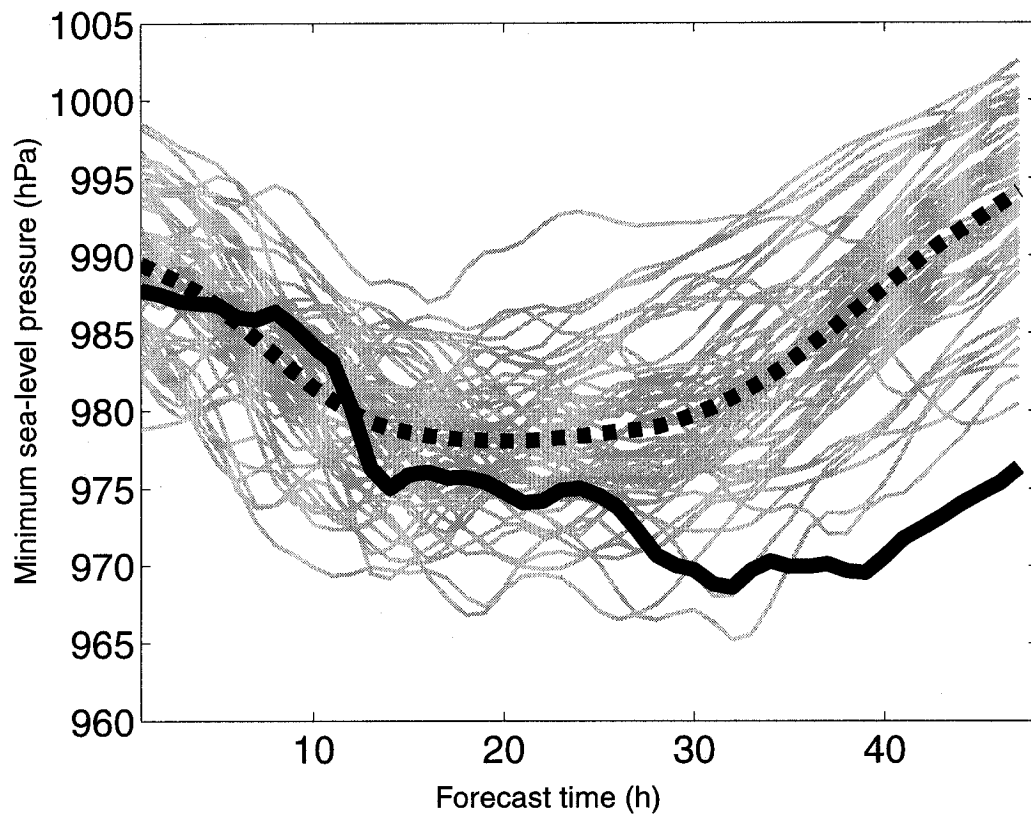


FIG. 6.2: Comparison of the TR minimum sea-level pressure time series and the CTL forecast for the same period referenced in fig 6.1.

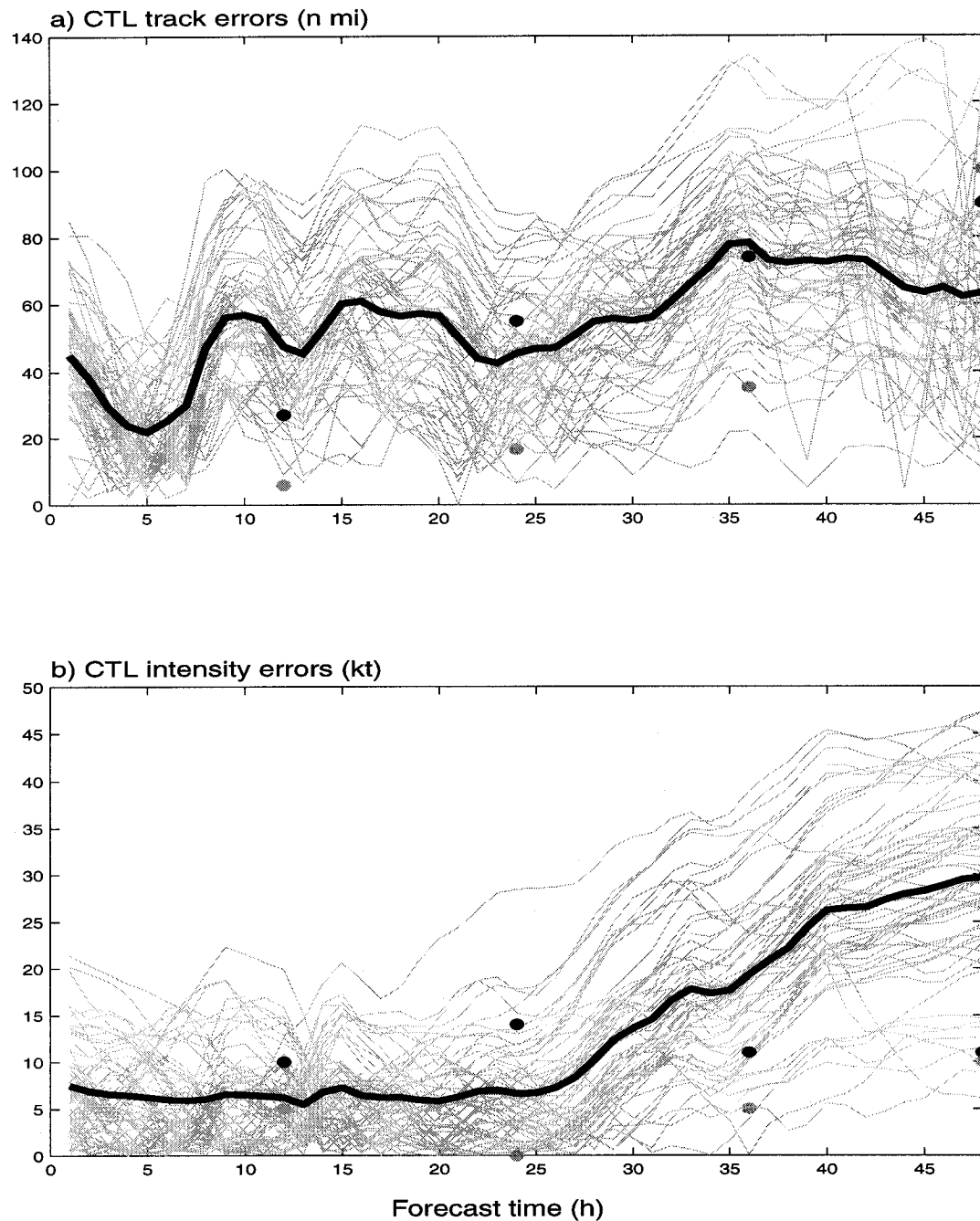


FIG. 6.3: Track (a) and intensity (b) errors for 48-hour forecast initialized with CTL ensemble at 12Z 28 October. Thin gray lines represent individual ensemble members, and the heavy black line represents the ensemble mean. 12, 24, 36 and 48 hour errors for the official NHC forecast are included for reference (black dots are the average over all forecasts made for Beta, and gray dots are errors associated with this specific forecast period).

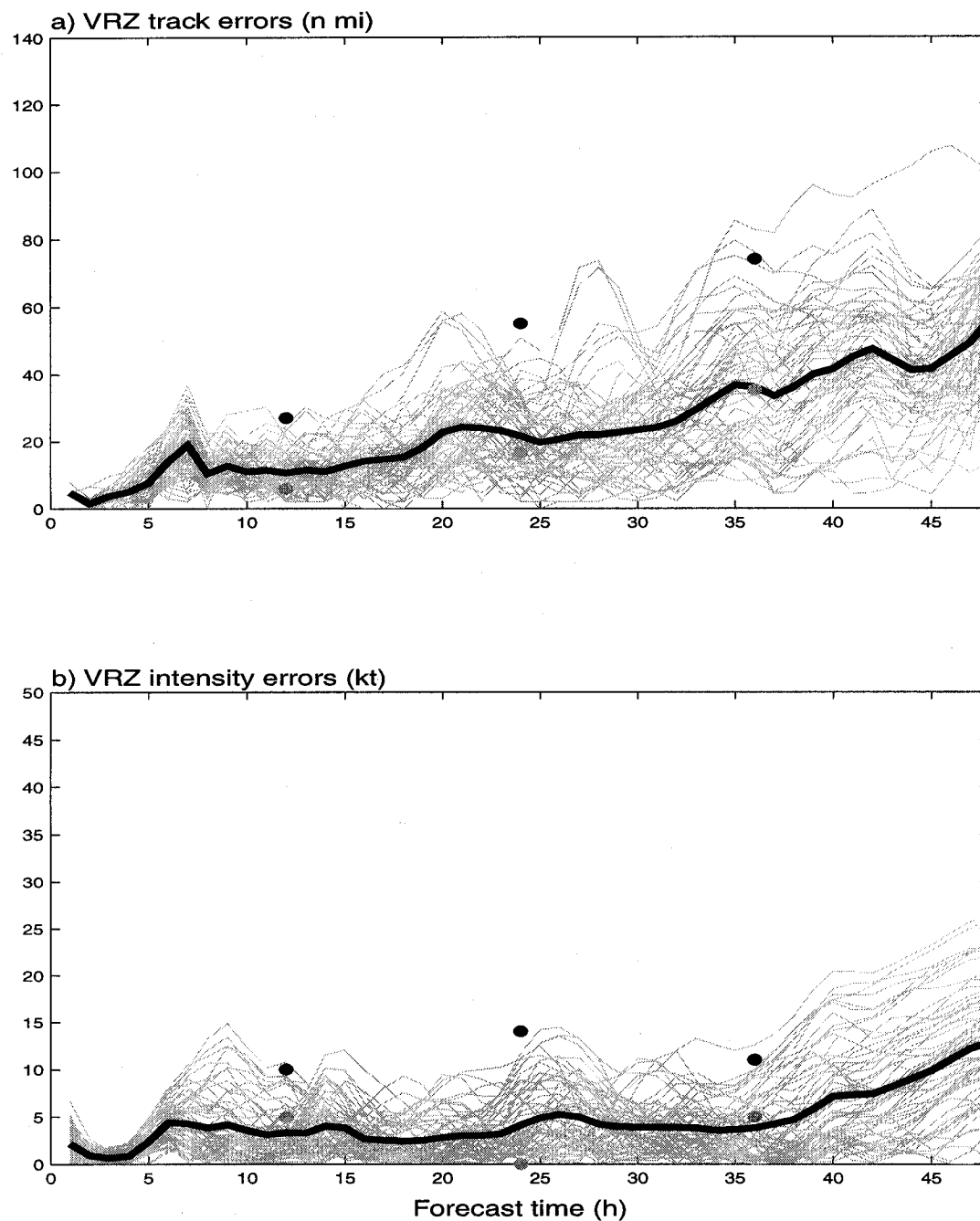


FIG. 6.4: As in figure 6.3, but for the forecast initiated from the VRZ analysis valid at 12Z 28 October.

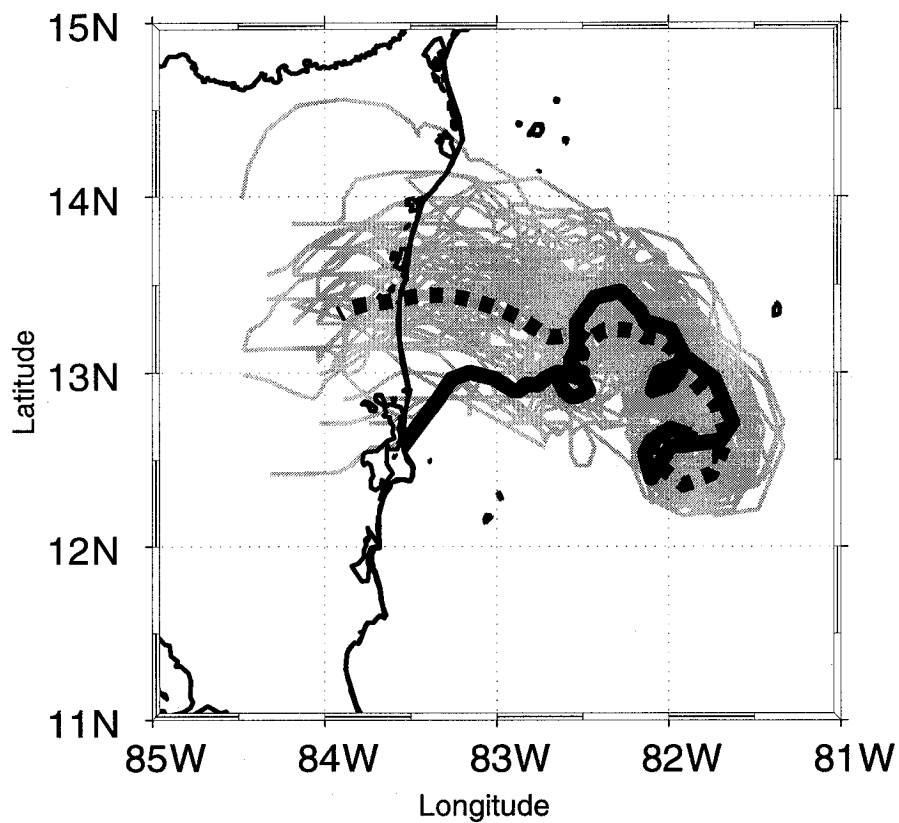


FIG. 6.5: Comparison of the TR track and the VRZ forecast for the period 12Z 28 October to 12Z 30 October. (Individual ensemble members are represented by thin gray lines and the ensemble mean by the heavy dashed line).

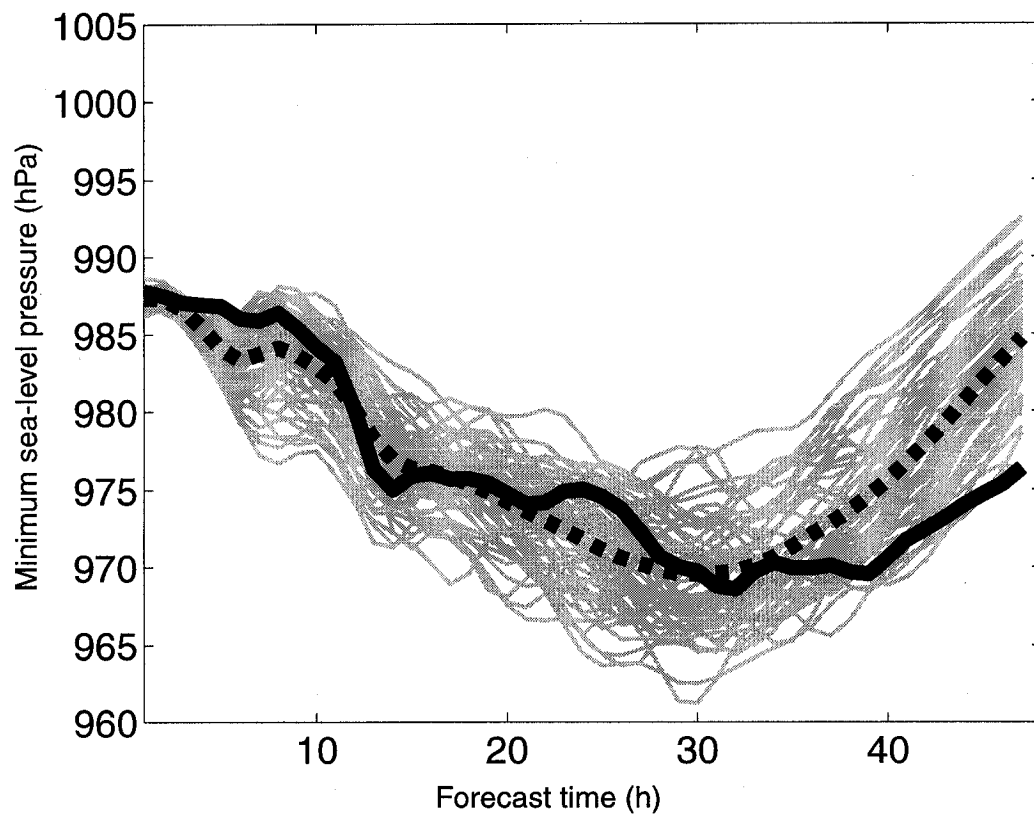


FIG. 6.6: Comparison of the TR minimum sea-level pressure time series and the VRZ forecast for the same period as referenced in fig 6.5.

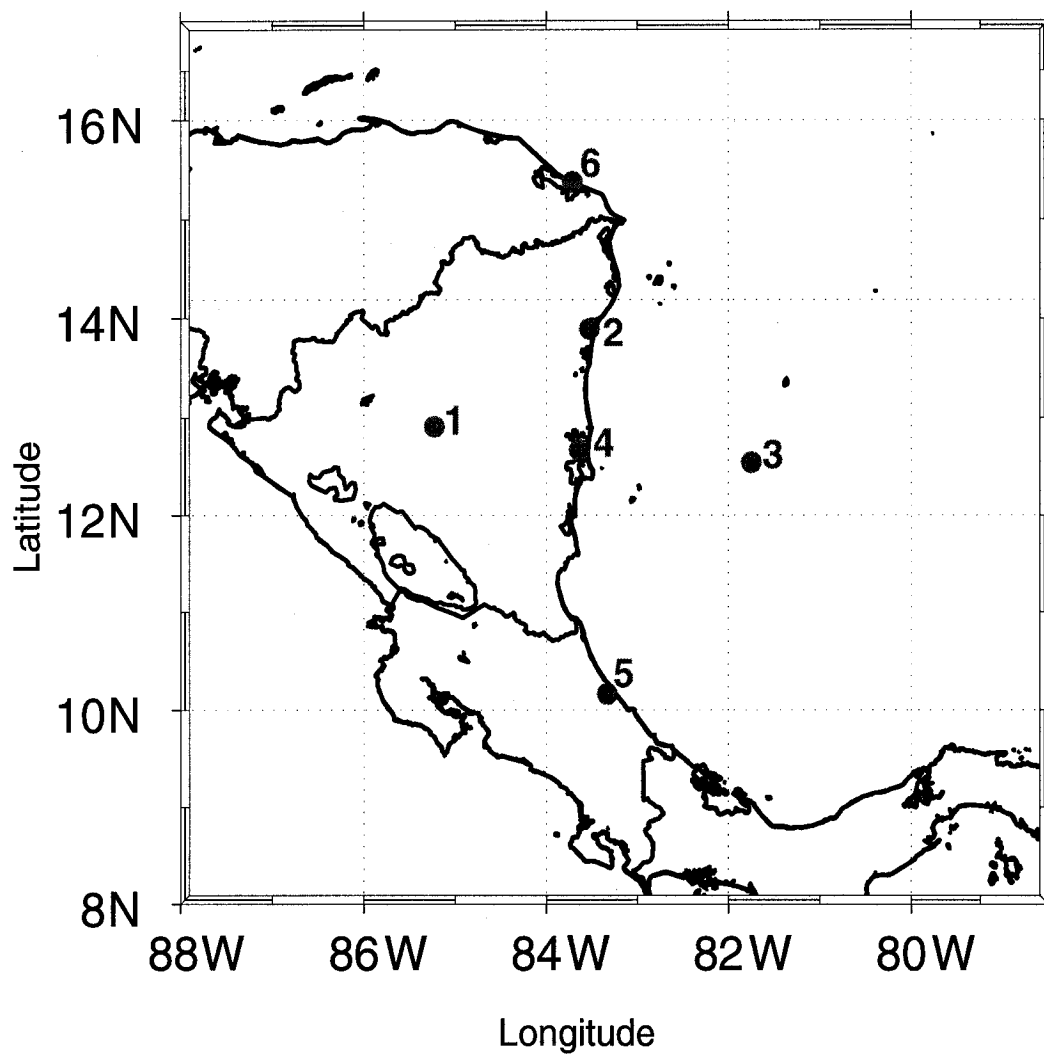


FIG. 6.7: Six surface stations for which time series of surface wind and rain rate are examined. 1 – Rio Blanco, Nicaragua; 2 – Puerto Cabezas, Nicaragua; 3 – San Andres Island; 4 – Landfall point of Beta in TR; 5 – Puerto Limon, Costa Rica; 6 – Puerto Lempira, Honduras.

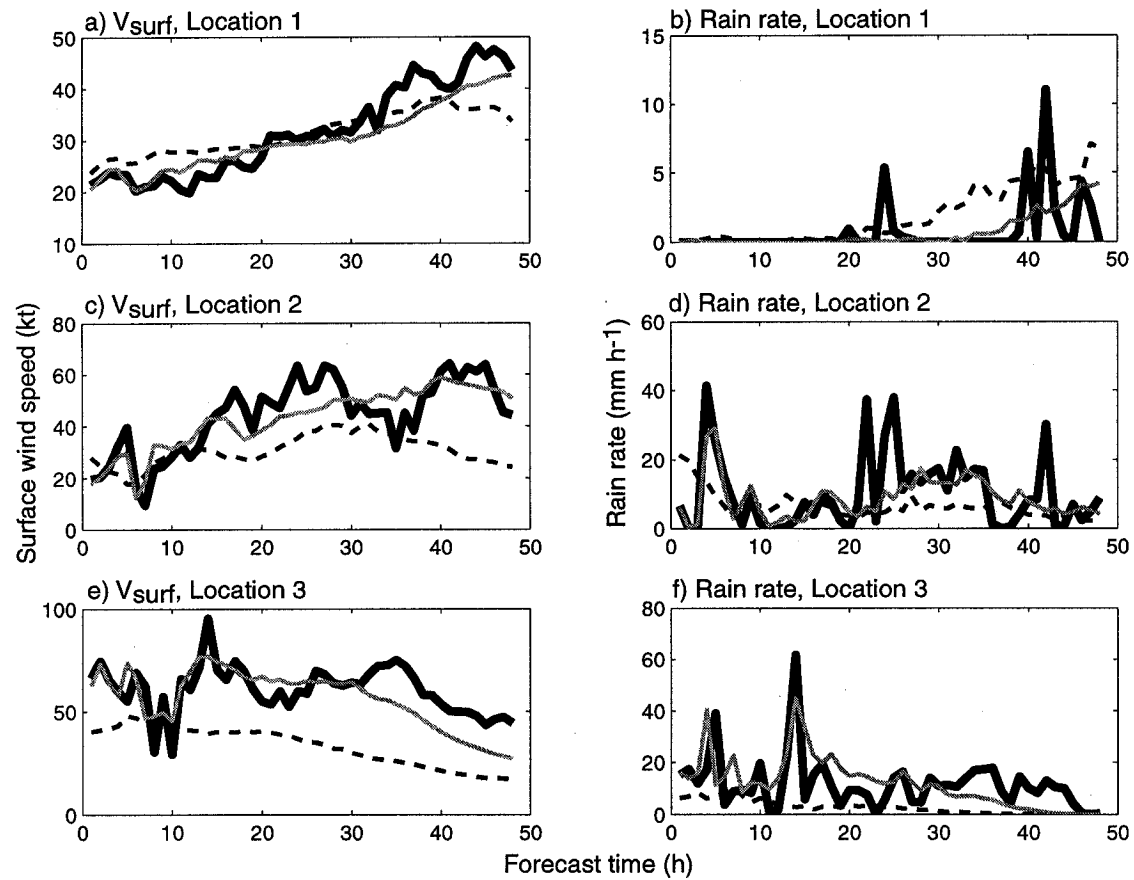


FIG. 6.8: Time series of surface wind and rain rate for the first three stations indicated in figure 6.7. (1 – Rio Blanco, Nicaragua; 2 – Puerto Cabezas, Nicaragua; 3 – San Andres Island.) TR is indicated by the thick solid line, CTL by the dashed line, and VRZ by the gray line.

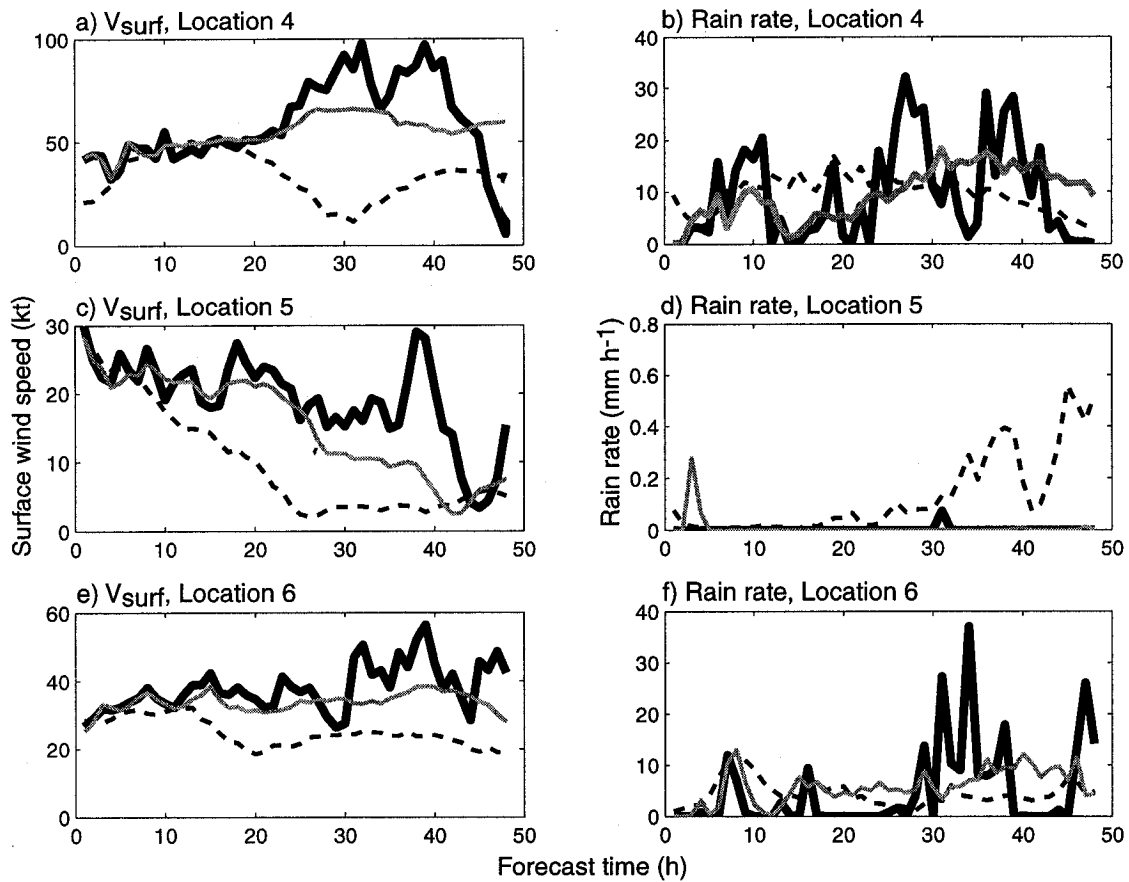


FIG. 6.8 cont.: Time series of surface wind and rain rate for stations 4 through 6. (4 – Landfall point of Beta in TR; 5 – Puerto Limon, Costa Rica; 6 – Puerto Lempira, Honduras.) TR is indicated by the thick solid line, CTL by the dashed line, and VRZ by the gray line.

TABLE 6.1: Pearson correlation coefficients between the truth simulation, TR, and the two simulations, CTL and VRZ, computed for the first (1-24) and second (25-48) halves of the forecast period. Also shown are the differences in correlation, $\Delta r = r_{VRZ} - r_{CTL}$. Values in bold indicate that Δr is significant at the 0.01 level.

Forecast	Correlation with TR for Forecast Period (h)	
	1-24	25-48
CTL V_{surf}	0.6848	0.4518
VRZ V_{surf}	0.9355	0.8481
Δr	0.2507	0.3963
CTL rain rate	0.2805	0.4332
VRZ rain rate	0.7133	0.5051
Δr	0.4328	0.0719

TABLE 6.2: Six threshold criteria used in computing Brier skill scores (BSS) for the VRZ forecast.

Threshold name	Criterion
w1	$V_{\text{surf}} > 34 \text{ kt}$
w2	$V_{\text{surf}} > 64 \text{ kt}$
w3	$V_{\text{surf}} > 84 \text{ kt}$
r1	Rain rate $> 0 \text{ mm h}^{-1}$
r2	Rain rate $> 12.5 \text{ mm h}^{-1}$
r3	Rain rate $> 25 \text{ mm h}^{-1}$

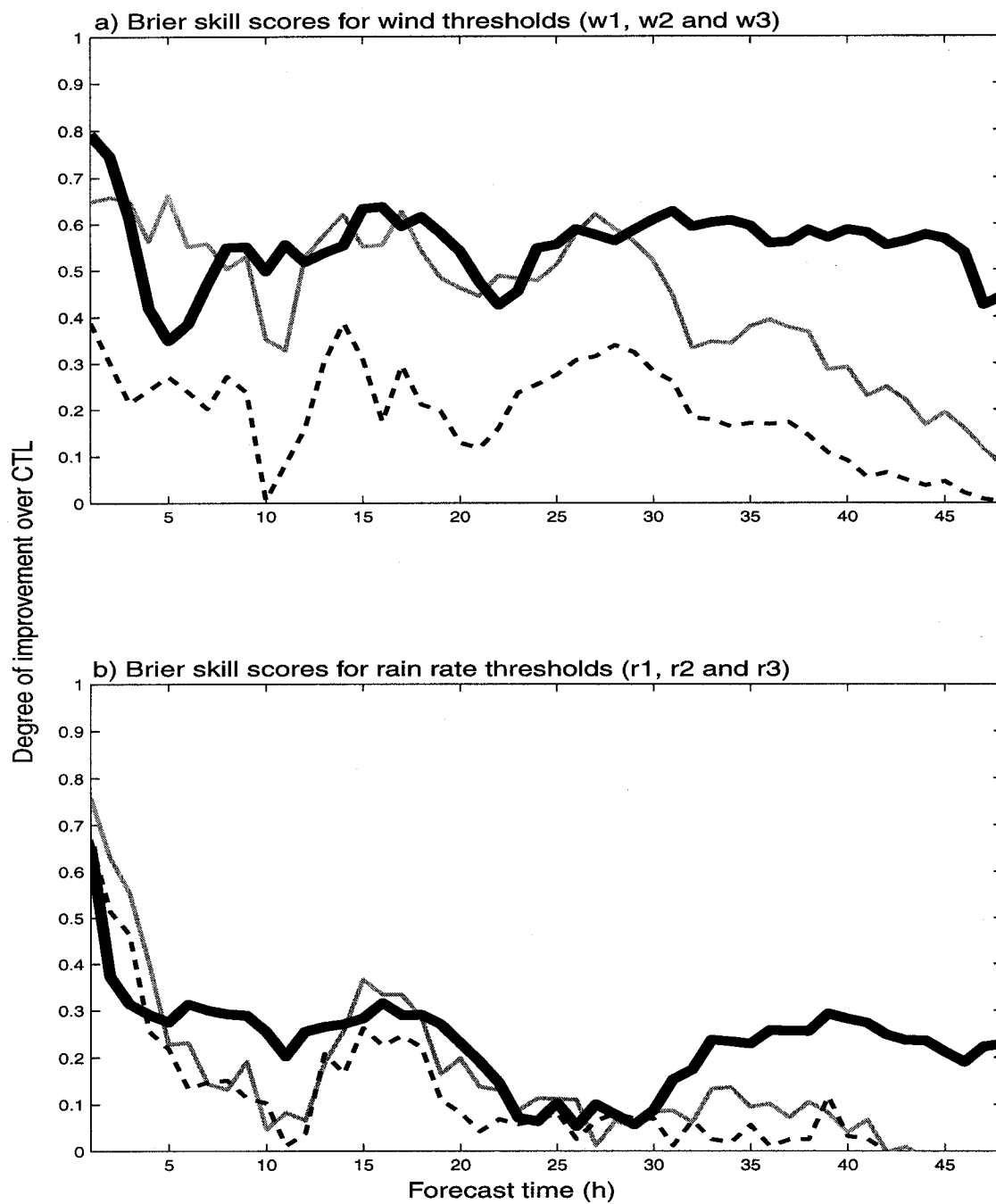


FIG. 6.9: Brier skill scores for the VRZ forecast (BSS_{VRZ}) for 3 wind thresholds (a) and three rain rate thresholds (b). (w1, r1 – thick solid line, w2, r2 – gray line, w3, r3 – dashed line). The wind and rain rate thresholds are summarized in table 6.2.

Chapter 7

Concluding Remarks and Future Work

It is not realistic to expect that any single observation source will offer an immediate resolution to the problem of forecasting tropical cyclone formation, intensity change and precipitation, the three constituent issues at the heart of the tropical cyclone problem as stated in chapter 1. However, it's also true that some observation types hold more promise than others for this purpose, and it has been demonstrated here that the Doppler radial velocity and radar reflectivity measured by NEXRAD In Space are indeed effective in significantly improving the representation of a developing tropical cyclone within the model analysis when assimilated using an ensemble Kalman filter. In particular, error reductions of up to 80 percent are achieved for the wind components, thermodynamic variable and condensate categories, with a somewhat more modest 45 percent achieved for the pressure variable.

Naturally, the purpose of producing better analyses is to produce better forecasts, and the results shown in chapter 6 demonstrate that a forecast initialized from the EnKF analysis exhibits enduring NIS impact over the 48-hour period to varying degrees. Track errors are reduced by 56 percent over the duration of the forecast (though only 10 percent at the final forecast time), and intensity errors are reduced 65 percent. While the track and intensity metrics are widely used in the tropical cyclone community to assess forecast skill, better choices involve examining the wind and rain at surface stations for which real forecasts might need to be made. In this context, the impact is seen to depend on the

threshold value of wind or rain being forecast. In general, forecasts of tropical storm force and hurricane force winds are 50 to 60 percent better than CTL over the first 24 hours and somewhat less thereafter, while improvement in rain forecasts ranges from 10 to 30 percent. The markedly poorer forecast performance with regard to rain is one of the more striking findings of this research, and the reason appears to be twofold. The first concerns the discrete distribution of rain over the grid and the tendency of phase errors to be multiplied. The second involves the predictability of the energy-containing disturbances which are forcing (and in turn being forced by) the rain processes. It is expected that this mechanism (and the error growth associated with it) will be even more pronounced at finer resolutions.

To put these findings in a more meaningful perspective, it will be necessary to perform a similar set of OSSE for currently available observation types such as microwave radiances, atmospheric motion vectors, scatterometer winds, etc. Only then can the quantitative and qualitative aspects of the impact be fully appreciated. However, as is alluded to in chapter 2, the combined spatiotemporal coverage and observation quality of NIS is currently unrivalled and would, in the author's view, be virtually impossible for any other single platform to beat. That being said, it is perhaps most important to emphasize that the power of model-based optimal state estimation lies in maximizing the impact of all available measurements and not just a small subset.

These results represent but the first step into the future landscape of tropical cyclone prediction. It is anticipated that continued advances in numerical models (and, perhaps more importantly, the computers on which they thrive) will make cloud-

resolving simulation of tropical cyclones rather routine by the time NIS is placed into orbit. Indeed, if Moore's Law (Moore, 1965) continues to hold true and computing power doubles every two years, the advent of operational cloud-resolving modeling on a global scale may be nearer than seemed possible only several years ago. With this eventuality in mind, it is critically important that data assimilation techniques be developed which are capable of combining state-of-the-art models and state-of-the-art observing technologies for optimal estimation of the atmospheric state at scales of one kilometer (or less).

To achieve this goal, ensemble techniques (such as the EnKF employed in this research) will need to be refined as they are applied to successively smaller scales. In particular, while an ensemble of rather modest size (e.g. 60 members) is capable of representing the essence of the pertinent atmospheric dynamics and its associated error structures at 13.6 km resolution, it is much less certain if a similarly sized ensemble would be capable of success at 1, 2 or even 5 km. It is the impression of the author that it would not. Whether 100 members would be sufficient, or whether 200 or 500 would be required, remains to be demonstrated. Investigation of this aspect of the combined tropical cyclone / ensemble-based NWP problem is therefore a priority and will require a significant expansion of modeling and assimilation efforts.

A similar expansion will be necessary to explore the performance of the EnKF across a much wider spectrum of cases. The tropical cyclone considered here was typical in most aspects, and while typical cases are just that, it is often the atypical cases that cause the most problems for forecasters (and thus stand to benefit the most from the improved state estimates proffered by data assimilation in general). Implicit in this need

for a more expansive treatment is an in-depth examination of tropical cyclogenesis and the difficulties associated with its prediction. Perhaps more so than any other aspect of the tropical cyclone problem, the genesis phase is a marvelous demonstration of scale interaction (Ritchie and Holland, 1997). As such, the assimilation tools must be capable of resolving error correlation structures across a range of scales, from individual clouds right up to planetary waves. This is a daunting task, and its ultimate success will clearly depend heavily on the work outlined above.

Finally, the inherently probabilistic character of the EnKF (as well as other ensemble- or particle-based methods) needs to be recognized and developed. This includes identification and exploitation of strengths as well as prescribing remedies for weaknesses. The fundamental machinery of the EnKF (i.e. linear estimation of a Gaussian random process) appears not to be problematic at the scales investigated here, and hence a two-moment approach to state estimation proves largely sufficient. However, at cloud-resolving scale, this may not be the case, and some remedy may need to be sought. A wealth of options, from relatively simple mixture models (Anderson and Anderson, 1999) to sophisticated evolutionary algorithms (e.g. Koza, 1992) are available and seem amenable to the problem at hand. Regardless of the method that ultimately finds favor, it must be used to convey the unsettling reality that forecasts may no longer be conceived of as deterministic truths. An appreciation of the associated uncertainty is critical. As Sir Karl Popper wrote some time ago:

“The old scientific ideal of *episteme* – of absolutely certain demonstrable knowledge – has proved to be an idol. The demand for scientific objectivity makes it

inevitable that every scientific statement must remain *tentative forever*. It may indeed be corroborated, but every corroboration is relative to other statements which, again, are tentative. Only in our subjective experiences of conviction, in our subjective faith, can we be absolutely certain.”

I doubt whether Popper had the data assimilation problem (or even the state estimation problem) in mind when he wrote those words, but it would be difficult to find a more succinct (or a more accurate) summation of the problem anywhere. Substituting “estimates” for “tentative” brings his statement still closer to our predicament, and in this form one can add that, though necessarily tentative, our state of knowledge about the future (and even the present) may yet be provided with bounds. Such limits, when well computed and fairly applied, provide something far from abject evidence of our inability to know. We may rather hope that they constrain our ignorance.

REFERENCES

Chapter 1

- Bender, M.A., Marchok, T., Ginis, I., Thomas, B. and I.-J. Moon, 2006: A summary of recent GFDL model upgrades and plans for 2006. Presented at the 27th AMS Conference on Hurricanes and Tropical Meteorology, Monterey, CA. 26 April, 2006.
- Beven, J.L., 2006: Blown away, the 2005 Atlantic hurricane season. *Weatherwise*, Jul/Aug, 32-44.
- Bucy, R.S. and K.D. Senne, 1971: Digital Synthesis of Nonlinear Filters. *Automatica*, **7**, 3, 287-289.
- Emanuel, K. A., 1986: An air-sea interaction theory for tropical cyclones. Part I: steady state maintenance. *J. Atmos. Sci.*, **43**, 585-605.
- Emanuel, K. A., 2005: Increasing destructiveness of tropical cyclones over the past 30 years. *Nature*, **436**, 686-688.
- Evensen, G., 1994: Sequential data assimilation with a nonlinear quasi-geostrophic model using Monte Carlo methods to forecast error statistics. *J. Geophys. Res.*, **99**, 10143-10162.
- Gray, W.M., 1979: *Hurricanes: Their formation, structure and likely role in the tropical circulation. Meteorology over the Tropical Oceans*. D.B. Shaw (ed), Royal Meteorological Society, James Glaisher House, Bracknell, Berkshire. 155-218.
- Gray, W.M., 2005: Comments on "Increasing destructiveness of tropical cyclones over the past 30 years" by Kerry Emanuel. ArXiv Physics e-prints, arXiv:physics/0601050.
- Holland, G.J., 1993: "Ready Reckoner" - Chapter 9, *Global Guide to Tropical Cyclone Forecasting*, WMO/TC-No. 560, Report No. TCP-31, World Meteorological Organization; Geneva, Switzerland
- Houze, R. A. Jr., S. S. Chen, B. F. Smull, W.-C. Lee, M. M. Bell, 2007: Hurricane intensity and eyewall replacement. *Science*, **315**, 1235-1239.

Im, E., E.A. Smith, S.L. Durden, S. Tanelli, J. Huang, Y. Rahmat-Samii, M. Lou, 2003: Instrument concept of NEXRAD in space (NIS) - a geostationary radar for hurricane studies. Geoscience and Remote Sensing Symposium 2003, IEEE International , **3**, 2146- 2148.

Kalman, R.E.,1960: A New Approach to Linear Filtering and Prediction Problems. *Journal of Basic Engineering*, Transactions of the ASME, D, **82** (1), 35-45.

Louie, Kin-sheun and Kam-biu Liu, 2003: Earliest historical records of typhoons in China. *Journal of Historical Geography*, **29** (3), 299-316.

Sumner, H.C., 1943: North Atlantic hurricanes and tropical disturbances of 1943. *Mon. Wea. Rev.*, **71**, 179-183.

Chapter 2

Brueske, K. F., and C. Velden, 2003: Satellite-based tropical cyclone intensity estimation using the NOAA-KLM series advanced microwave sounding unit (AMSU). *Mon. Wea. Rev.*, **131**, 687-697.

Hobbs, P.V., N.T. Funk, R.R. Weiss, Sr., J.D. Locatelli, and K.R. Biswas, 1985: Evaluation of 35 GHz radar for cloud physics research. *J. Atmos. Ocean. Tech.*, **2**, 35-48.

Lin, J.K.H., H. Fang, E. Im and U.O. Quijano, 2006: Concept study of a 35-m spherical reflector system for NEXRAD in space application. 47th AIAA/ASME/ASCE/AHS/ASC Structures, Structural Dynamics, and Materials Conference, American Institute of Aeronautics and Astronautics. 1-4 May, 2006, Newport, RI.

Chapter 3

Pasch, R.J. and D.P. Roberts, 2006: Tropical cyclone report, Hurricane Beta, 26-31 October 2005. National Hurricane Center, Miami, FL.

Chapter 4

Anderson, B.D.O. and Moore, J.B., 2005: *Optimal Linear Filtering*. Dover Publications, NY, 357 pp.

- Evensen, G., 1994: Sequential data assimilation with a nonlinear quasi-geostrophic model using Monte Carlo methods to forecast error statistics. *J. Geophys. Res.*, **99**, 10143-10162.
- Evensen, G., 2003: The ensemble Kalman filter: theoretical formulation and practical considerations. *Ocean Dynamics*, **53**, 343-367.
- Gaspari, G. and S.E. Cohn, 1999: Construction of correlation functions in two and three dimensions. *Quart. J. Roy. Meteor. Soc.*, **125**, 723-757
- Houtekamer, P.L. and Mitchell, H.L., 1998: data assimilation using an ensemble Kalman filter technique. *Mon. Wea. Rev.*, **126**, 796-811.
- Smith, P.L., C.G. Myers, and H.D. Orville, H.D., 1975: Radar reflectivity factor calculations in numerical cloud models using bulk parameterizations of precipitation processes. *J. Appl. Meteor.*, **14**, 1156-1165.
- Smith, P.L., 1984: Equivalent radar reflectivity factors for snow and ice particles. *J. Appl. Meteor.*, **23**, 1258-1260.
- Tong, M. and M. Xue, 2005: Ensemble Kalman filter assimilation of radar data with a compressible nonhydrostatic model: OSS experiments. *Mon. Wea. Rev.*, **133**, 1789-1807.
- Torn, R.D., G. J. Hakim and C. Snyder, 2006: Boundary conditions for limited-area ensemble Kalman filters. *Mon. Wea. Rev.*, **134**, 2490-2502.
- Tripoli, G.J. and W.R. Cotton, 1981: The use of ice-liquid potential temperature as a thermodynamic variable in deep atmospheric models. *Mon. Wea. Rev.*, **109**, 1094-1102.
- Tripoli, G.J., 1992: A nonhydrostatic mesoscale model designed to simulate scale interaction. *Mon. Wea. Rev.*, **120**, 1342-1359.

Chapter 5

- Bender, M.A., R.J. Ross, R.E. Tuleya, and Y. Kurihara, 1992: Improvements in tropical cyclone track and intensity forecasts using the GFDL initialization system. *Mon. Wea. Rev.*, **121**, 2046-2061.

Chapter 6

Blalock, H., 1979: *Social Statistics*. McGraw-Hill, NY, 592 pp.

Brier, G. W., 1950: Verification of forecasts expressed in terms of probability. *Mon. Wea. Rev.*, **78**, 1-3.

Chapter 7

Anderson, J.L. and S.L. Anderson, 1999: A Monte Carlo implementation of the nonlinear filtering problem to produce ensemble assimilations and forecasts. *Mon. Wea. Rev.*, **127**, 2741–2758.

Koza, J.R., 1992: *Genetic programming: on the programming of computers by means of natural selection*, MIT Press, Cambridge, MA, 840 pp.

Moore, G.E., 1965: Cramming more components onto integrated circuits. *Electronics*, **38**(8), 114-117.

Popper, K., 1959: *The logic of scientific discovery*, Routledge Press, New York, NY, 544 pp.

Ritchie, E.A. and G.J. Holland, 1997: Scale interactions during the formation of typhoon Irving. *Mon. Wea. Rev.*, **125**, 1377–1396